Breakup in nucleon-deuteron scattering with Δ-isobar excitation

K. Chmielewski,[1,*] A. Deltuva,[1,†] A. C. Fonseca,[2] S. Nemoto,[3] and P. U. Sauer[1]
[1]*Institut für Theoretische Physik, Universität Hannover, D-30167 Hannover, Germany*
[2]*Centro de Física Nuclear da Universidade de Lisboa, P-1649-003 Lisboa, Portugal*
[3]*Department of Physics, Faculty of Science and Technology, Science University of Tokyo, Noda, Chiba 278, Japan*
(Received 8 July 2002; published 22 January 2003)

Breakup in nucleon-deuteron scattering is described. The description is based on a coupled-channel two-baryon potential that allows for the virtual excitation of a nucleon to a Δ isobar. The Coulomb interaction is not included. Channel coupling gives rise to an effective three-nucleon force. The three-particle scattering equations are solved by real-axis integration using a separable expansion of the two-baryon transition matrix. Examples for spin-averaged and spin-dependent observables are calculated and compared with experimental data.

DOI: 10.1103/PhysRevC.67.014002 PACS number(s): 21.45.+v, 21.30.−x, 25.10.+s, 24.70.+s

I. INTRODUCTION

This paper is the third in a series on nucleon-deuteron scattering. The first one [1], called paper I, establishes a separable expansion for the underlying two-baryon interaction [2], which explicitly allows for Δ-isobar excitation. The second one [3], called paper II, uses that separable expansion of the coupled-channel transition matrix for the calculation of elastic nucleon-deuteron scattering, below and above three-nucleon breakup. This paper does so for inelastic nucleon-deuteron scattering, i.e., for three-nucleon breakup. The Δ isobar gives rise to an effective three-nucleon force. The calculation is without Coulomb interaction. Thus, it refers to breakup in neutron-deuteron scattering, though the comparison is mostly with data of proton-deuteron scattering.

The theoretical description of elastic nucleon-deuteron scattering up to about 150 MeV nucleon lab energy in terms of realistic two-nucleon potentials has been generally quite successful [4,5] with the following exceptions.

(1) At low energies the description of scattering observables and of bound-state properties are correlated. An appropriate three-nucleon force has to be added to account for trinucleon binding in full.

(2) The description of proton-deuteron scattering at very low energies for most angles and at higher energies predominantly in forward direction requires the inclusion of the Coulomb interaction between the protons.

(3) There are long-standing discrepancies in the spin observables $A_y(n)$ and iT_{11} around 10 MeV neutron lab energy. Furthermore, without a three-nucleon force, the minimum of the unpolarized differential cross section beyond 65 MeV nucleon lab energy cannot be accounted for; this fact is called Sagara discrepancy.

Paper II and Ref. [6] study the effect of the Δ isobar on elastic nucleon-deuteron scattering. The effect is usually small; at most, modest for some spin observables at higher energies. Reference [6] finds a beneficial Δ-isobar effect on the Sagara discrepancy. The Δ isobar is not helpful for the spin observables $A_y(n)$ and iT_{11} around 10 MeV neutron lab energy.

This paper extends the description to spin-averaged and spin-dependent observables of breakup in nucleon-deuteron scattering. Experimental data for breakup are much scarcer than for elastic scattering. Kinematical regimes in which the three-nucleon force mediated by the Δ isobar may play a determining role are searched for. The theoretical description requires a change of technique when solving the three-particle scattering equations compared with paper II, which employed a contour deformation technique. Real-axis integration is used instead. The technique is developed in the present context.

In Sec. II basic features of the calculation are described; however, the important technical details are deferred to the Appendix. Section III presents our results for spin-averaged and spin-dependent observables of breakup in inelastic nucleon-deuteron scattering. The conclusions are given in Sec. IV.

II. BASIC FEATURES OF THE CALCULATION

The notation is taken over from paper I and is assumed to be self-evident; explanations of the notation are kept to a minimum.

A. Alt-Grassberger-Sandhas (AGS) breakup equation

The symmetrized break-up transition matrix $U_0(Z)$ is defined in Eq. (2.13) of paper I according to

$$U_0(Z) = G_0^{-1}(Z) + [1 + T_\alpha(Z) G_0(Z)] U(Z). \qquad (1a)$$

It is obtained from the symmetrized multichannel transition matrix $U(Z)$,

$$U(Z) = P G_0^{-1}(Z) + P T_\alpha(Z) G_0(Z) U(Z), \qquad (1b)$$

given in Eq. (2.12) of the same paper. Using Eq. (1b) once more, we rewrite the standard quadrature for the breakup transition matrix as follows:

*Electronic address: Karsten.Chmielewski@itp.uni-hannover.de
†On leave from Institute of Theoretical Physics and Astronomy, Vilnius University, Vilnius 2600, Lithuania.

$$U_0(Z)=(1+P)G_0^{-1}(Z)+(1+P)T_\alpha(Z)G_0(Z)U(Z), \tag{2}$$

where $G_0(Z)$ is the free resolvent, $P=P_{123}+P_{321}$ the permutation operator, and $T_\alpha(Z)$ the two-baryon coupled-channel transition matrix between the baryons β and γ in the three-particle space, $(\alpha\beta\gamma)$ cyclic. The free Hamiltonian in $G_0(Z)$ does not contain center of mass (c.m.) motion, but baryon rest masses, normalized to zero for three nucleons. The channel states $|\phi_\alpha(\mathbf{q})\nu_\alpha\rangle$ and $|\phi_0(\mathbf{pq})\nu_0\rangle$ are defined in paper I, $\mathbf{p}$ and $\mathbf{q}$ are the internal Jacobi momenta, ν_α and ν_0 are sets of discrete quantum numbers determining the channel states in full. Both channel states are antisymmetrized with respect to the pair $(\beta\gamma)$. $|\phi_\alpha(\mathbf{q}_i)\nu_{\alpha_i}\rangle$ is the initial nucleon-deuteron state with the initial c.m. energy $E_i=e_d+\mathbf{q}_i^2/2M_\alpha$, e_d being the deuteron binding energy, $M_\alpha=2m_N/3$ the reduced spectator mass, and m_N the nucleon rest mass. $|\phi_0(\mathbf{pq})\nu_0\rangle$ is the final three-nucleon breakup state. It is given in paper I as a coupled state with respect to pair spin and isospin. However, the final state is measured in the uncoupled form, i.e.,

$$|\phi_0(\mathbf{p}_f\mathbf{q}_f)\nu_0(m_f)\rangle=\frac{1-P_{\beta\gamma}}{\sqrt{2}}|\mathbf{p}_f\mathbf{q}_f\rangle_\alpha|s_\alpha m_{s_{\alpha_f}} t_\alpha m_{t_{\alpha_f}} b_{\alpha_f}\rangle|s_\beta m_{s_{\beta_f}} t_\beta m_{t_{\beta_f}} b_{\beta_f}\rangle|s_\gamma m_{s_{\gamma_f}} t_\gamma m_{t_{\gamma_f}} b_{\gamma_f}\rangle, \tag{3a}$$

$$|\phi_0(\mathbf{p}_f\mathbf{q}_f)\nu_0(m_f)\rangle=\sum_{S_f M_{s_f} T_f M_{T_f}}|\phi_0(\mathbf{p}_f\mathbf{q}_f)\nu_{0_f}\rangle\langle s_\beta m_{s_{\beta_f}} s_\gamma m_{s_{\gamma_f}}|S_f M_{S_f}\rangle\langle t_\beta m_{t_{\beta_f}} t_\gamma m_{t_{\gamma_f}}|T_f M_{T_f}\rangle. \tag{3b}$$

The discrete quantum numbers of the final state are explained in Fig. 2 of paper I. Its c.m. energy is $E_f=\mathbf{p}_f^2/2\mu_\alpha+\mathbf{q}_f^2/2M_\alpha$ with the reduced pair mass $\mu_\alpha=m_N/2$.

The S matrix for breakup is given by the symmetrized on-shell breakup transition matrix $U_0(Z)$, i.e.,

$$\langle\phi_0(\mathbf{p}_f\mathbf{q}_f)\nu_0(m_f)|S|\phi_\alpha(\mathbf{q}_i)\nu_{\alpha_i}\rangle=-2\pi i\delta(E_f-E_i)\langle\phi_0(\mathbf{p}_f\mathbf{q}_f)\nu_0(m_f)|U_0(E_i+i0)|\phi_\alpha(\mathbf{q}_i)\nu_{\alpha_i}\rangle. \tag{4}$$

When determining the S matrix the initial and final states are fully antisymmetrized and normalized through $(1+P)/\sqrt{3}$; however, those symmetrization operators are incorporated into the definition of the symmetrized breakup transition matrix $U_0(Z)$ of paper I. The on-shell transition matrix $U_0(Z)$ is calculated according to Eq. (2).

B. Separable expansion of coupled-channel interaction and AGS breakup equation

The form (2) of the breakup transition matrix $U_0(Z)$ is especially convenient, when the two-baryon transition matrix $T_\alpha(Z)$ is separably expanded according to our general strategy for solving the AGS three-particle scattering equations. The separable expansion

$$T_\alpha(Z)=|\mathbf{g}_\alpha\rangle\mathbf{T}_\alpha(Z)\langle\mathbf{g}_\alpha| \tag{5a}$$

yields for $U_0(Z)$,

$$U_0(Z)=(1+P)G_0^{-1}(Z)+(1+P)|\mathbf{g}_\alpha\rangle\mathbf{T}_\alpha(Z)\times\langle\mathbf{g}_\alpha|G_0(Z)U(Z). \tag{5b}$$

Since the deuteron state defines one element, labeled i_0, in the form factor $|\mathbf{g}_\alpha\rangle$ of the separable expansion (5a), $\mathbf{T}_\alpha(Z)$ being the corresponding propagator, the initial nucleon-deuteron state can be rewritten as

$$|\phi_\alpha(\mathbf{q}_i)\nu_{\alpha_i}\rangle=G_0(E_i+i0)|g_\alpha^{(i_0\pi_0 I_0 T_0)}M_{I_i}M_{T_0}\rangle|\mathbf{q}_i s_0 m_{s_i} t_0 m_{t_0} b_0\rangle_\alpha. \tag{6}$$

Thus, the breakup S matrix (4) based on the breakup transition matrix $U_0(Z)$ in the form (2) needs the matrix elements of the operator $\langle\mathbf{g}_\alpha|G_0(Z)U(Z)G_0(Z)|\mathbf{g}_\alpha\rangle$ half-shell. Paper II calculated the same operator on shell for the description of elastic nucleon-deuteron scattering.

C. Solution of the integral equation for the half-shell transition matrix $\langle\mathbf{g}_\alpha|G_0(Z)U(Z)G_0(Z)|\mathbf{g}_\alpha\rangle$

The transition matrix $\langle\mathbf{g}_\alpha|G_0(E_i+i0)U(E_i+i0)G_0(E_i+i0)|\mathbf{g}_\alpha\rangle$ is required half-shell for the on-shell breakup amplitude $U_0(E_i+i0)|\phi_\alpha(\mathbf{q}_i)\nu_{\alpha_i}\rangle$ according to Eqs. (5b) and (6). It is obtained by solving the integral equation

$$\langle\mathbf{g}_\alpha|G_0(Z)U(Z)G_0(Z)|\mathbf{g}_\alpha\rangle=\langle\mathbf{g}_\alpha|PG_0(Z)|\mathbf{g}_\alpha\rangle+\langle\mathbf{g}_\alpha|PG_0(Z)|\mathbf{g}_\alpha\rangle\mathbf{T}_\alpha(Z)\times\langle\mathbf{g}_\alpha|G_0(Z)U(Z)G_0(Z)|\mathbf{g}_\alpha\rangle. \tag{7}$$

The kernel $\langle\mathbf{g}_\alpha|PG_0(Z)|\mathbf{g}_\alpha\rangle\mathbf{T}_\alpha(Z)$ of the integral equation (7) contains singularities: $\langle\mathbf{g}_\alpha|PG_0(Z)|\mathbf{g}_\alpha\rangle$ develops so-called *moving* singularities of kinematical origin above the breakup threshold, whereas the propagator $\mathbf{T}_\alpha(Z)$ contains

the deuteron bound-state pole. The arising of these singularities was discussed in depth in paper II which employed the method of contour deformation for dealing with them. That method was adequate for the calculation of on-shell matrix elements needed for the description of elastic scattering in paper II, but it was already tedious there. For breakup calculations that method gets even more tedious. It requires at least two distinct complex paths, and those paths have to be different for different available energies E_i. Contour deformation for breakup has not been numerically successful in the past. It was also tried by us tentatively, but problems of stability convinced us to develop the alternative technique of real-axis integration for solving Eq. (7). Its implementation rests on three technical pillars: spline interpolation, numerical evaluation of the singular integrals by specially calculated weights, and Padé approximation.

The details of the method are described in the Appendix; all items have novel aspects. The reliability of the technique is tested by comparing results for elastic nucleon-deuteron scattering which were obtained with the contour-deformation technique in paper II. In fact, all results given there in plots were recalculated using the real-axis technique. No differences, visible in plots, could be found, except minute ones for some spin observables of particularly small magnitude. Hence, no samples of that comparison are shown in this paper. The reliability check is an internal one for elastic nucleon-deuteron scattering; the comparison is possible for the coupled-channel interaction with Δ-isobar excitation employed [2] and for its purely nucleonic reference potential, the Paris potential [7]. The method of real-axis integration can without technical change be carried over from elastic nucleon-deuteron scattering to breakup. Furthermore, in the case of the purely nucleonic Paris potential, the comparison is also possible with the breakup results of Ref. [5]. This comparison turned out to be quite satisfactory. Thus, we consider our technique of real-axis integration highly reliable, and we employ it in this paper for calculating breakup in nucleon-deuteron scattering and for studying Δ-isobar effects in that process.

D. Observables of nucleon-deuteron breakup

The calculations of this paper are entirely nonrelativistic. Nevertheless, we like to make the step to observables by starting out from the relativistic form of the cross section,

$$d\sigma_{i\to f}=|\langle f|\mathcal{M}|i\rangle|^2\frac{d\mathrm{Lips}(k_{\alpha_i}+k_d,k_{\alpha_f},k_{\beta_f},k_{\gamma_f})}{4c^2\sqrt{(k_{\alpha_i}\cdot k_d)^2-m_N^2m_d^2c^4}}. \quad (8a)$$

The reason is that we carry out corresponding calculations of electromagnetic processes; for them the relativistic form of the cross section has important conceptual advantages. In Eq. (8a) $\langle f|\mathcal{M}|i\rangle$ is the Lorentz-invariant singularity-free matrix element, $d\mathrm{Lips}(k_{\alpha_i}+k_d,k_{\alpha_f},k_{\beta_f},k_{\gamma_f})$ the Lorentz-invariant phase space element of the final state defined in Eq. (11), and $4c^2\sqrt{(k_{\alpha_i}\cdot k_d)^2-m_N^2m_d^2c^4}$ a Lorentz-invariant factor containing the initial-state information.

We use the cross section (8a) in the lab system. The target deuteron is at rest, i.e., $\mathbf{k}_d=0$, the impinging nucleon has momentum $\mathbf{k}_{\alpha_i}$, which defines the z direction. The changes that arise when the deuteron impinges on a nucleon target are obvious. The matrix element $\langle f|\mathcal{M}|i\rangle$ of Eq. (8a) should be derived from a fully relativistic description of hadron dynamics. We are unable to give such a relativistic description. The nonrelativistic hadron dynamics employed is based on a two-baryon potential, fitted to data with the nonrelativistic form of the cross section in contrast to Eq. (8a), it connects the S matrix with the symmetrized on-shell breakup transition matrix $U_0(E_i+i0)$ in Eq. (4); it uses nonrelativistic energies for E_i and E_f. When, nevertheless, that breakup transition matrix is taken for an approximate construction of $\langle f|\mathcal{M}|i\rangle$, ignoring the difference in kinetic energies for a relativistic S matrix and its nonrelativistic correspondence of Eq. (4), the following identification is obtained:

$$\langle f|\mathcal{M}|i\rangle=\langle\phi_0(\mathbf{p}_f\mathbf{q}_f)\nu_0(m_f)|U_0(E_i+i0)|\phi_\alpha(\mathbf{q}_i)\nu_{\alpha_i}\rangle \times\frac{(2\pi\hbar)^{9/2}}{\hbar c}\sqrt{2k^0_{\alpha_i}c2k^0_dc2k^0_{\alpha_f}c2k^0_{\beta_f}c2k^0_{\gamma_f}c}. \quad (8b)$$

The calculation of $\langle\phi_0(\mathbf{p}_f\mathbf{q}_f)\nu_0(m_f)|U_0(E_i+i0)|\phi_\alpha(\mathbf{q}_i)\nu_{\alpha_i}\rangle$ uses the available initial c.m. energy E_i and the Jacobi momenta $\mathbf{q}_i$, $\mathbf{p}_f$, and $\mathbf{q}_f$; their relations to the single particle lab momenta are

$$E_i=e_d+\frac{\mathbf{k}^2_{\alpha_i}}{3m_N}, \quad (9a)$$

$$\mathbf{q}_i=-\frac{2}{3}\mathbf{k}_{\alpha_i}, \quad (9b)$$

$$\mathbf{p}_f=\frac{1}{2}(\mathbf{k}_{\beta_f}-\mathbf{k}_{\gamma_f}), \quad (9c)$$

$$\mathbf{q}_f=(\mathbf{k}_{\beta_f}+\mathbf{k}_{\gamma_f})-\frac{2}{3}\mathbf{k}_{\alpha_i}. \quad (9d)$$

The employed nonrelativistic dynamics is Galilean invariant. This implies that the matrix element $\langle f|\mathcal{M}|i\rangle$ is frame dependent. The frame dependence of Eq. (8b) is due to the energy factors $\sqrt{2k^0_{\alpha_i}c2k^0_dc2k^0_{\alpha_f}c2k^0_{\beta_f}c2k^0_{\gamma_f}c}$; they arise, rather artificially in Eq. (8b), since corresponding factors have to be attached to the phase space part of the cross section (8a). We note that already at 65 MeV nucleon lab energy the difference between lab and c.m. system amounts to a frame dependence of 2.5% for $\langle f|\mathcal{M}|i\rangle$. For the description of spin-averaged and spin-dependent cross sections the breakup transition matrix $U_0(E_i+i0)$ is conveniently abbreviated by the scattering amplitude $M(E_i\mathbf{p}_f\mathbf{q}_f)$,

$$\langle\phi_0(\mathbf{p}_f\mathbf{q}_f)\nu_0(m_f)|U_0(E_i+i0)|\phi_\alpha(\mathbf{q}_i)\nu_{\alpha_i}\rangle =\langle m_{s_{\alpha_f}}m_{s_{\beta_f}}m_{s_{\gamma_f}}|M(E_i\mathbf{p}_f\mathbf{q}_f)|M_{I_i}m_{s_i}\rangle, \quad (10)$$

in which the dependence on the spin projections of the particles in the initial and final states is made explicit. The neutron and proton nature of the nucleons $(\alpha\beta\gamma)$ in the final state is notationally not indicated, but always determined by experiment.

In contrast to the matrix element $\langle f|\mathcal{M}|i\rangle$ that carries the dynamics, the kinematical factors in Eq. (8a), i.e., the Lorentz-invariant phase-space element

$$d\mathrm{Lips}(k_{\alpha_i}+k_d,k_{\alpha_f},k_{\beta_f},k_{\gamma_f}) = (2\pi\hbar)^4\delta^{(4)}(k_{\alpha_f}+k_{\beta_f}+k_{\gamma_f}-k_{\alpha_i}-k_d) \times\frac{d^3k_{\alpha_f}d^3k_{\beta_f}d^3k_{\gamma_f}}{(2\pi\hbar)^9 2k^0_{\alpha_f}c\,2k^0_{\beta_f}c\,2k^0_{\gamma_f}c} \tag{11}$$

and the factor $4c^2\sqrt{(k_{\alpha_i}\cdot k_d)^2-m_N^2m_d^2c^4}$, which contains the incoming flux, the target density, and projectile and target normalization factors, could, in principle, be calculated relativistically. We shall not use that option in this paper; we believe that it is not justified; we discuss the reason in more detail in Sec. II E.

The momenta in the initial and final states are constrained by energy and momentum conservation. For example, if the momentum $\mathbf{k}_{\beta_f}$ and the direction $\hat{\mathbf{k}}_{\gamma_f}$ were measured, all three nucleon momenta are determined in the final state, although not always uniquely. In practice, the two nucleon scattering angles with respect to the beam direction $(\theta_\beta,\varphi_\beta)$ and $(\theta_\gamma,\varphi_\gamma)$, usually notationally shortened to $(\theta_\beta,\theta_\gamma,\varphi_\gamma-\varphi_\beta)$, and their kinetic energies without rest masses, E_{β_f} and E_{γ_f}, are meassured. Those energies are related by momentum and energy conservation and therefore lie on a fixed kinematical curve. The observables are therefore given as functions of the arclength S along that curve, i.e.,

$$S=\int_0^S dS \tag{12}$$

with $dS=\sqrt{dE^2_{\beta_f}+dE^2_{\gamma_f}}$ and E_{γ_f} being considered a function of E_{β_f} or vice versa depending on numerical convenience. The arclength is always taken counterclockwise along the kinematical curve. No confusion between the arclength S and the S matrix of Eq. (4) should arise. The normalization of the arclength value zero is chosen differently in different kinematical situations.

The lab cross section therefore takes the compact form

$$d\sigma_{i\to f}=|\langle m_{s_{\alpha_f}}m_{s_{\beta_f}}m_{s_{\gamma_f}}|M(E_i\mathbf{p}_f\mathbf{q}_f)|M_{I_i}m_{s_i}\rangle|^2 \times\mathrm{fps}\,dSd^2\hat{\mathbf{k}}_{\beta_f}d^2\hat{\mathbf{k}}_{\gamma_f} \tag{13a}$$

with the abbreviation fps for the phase-space factor. Using relativistic kinematics it takes the following form, i.e.,

$$\mathrm{fps}=(2\pi)^4\hbar^2\frac{k^0_{\alpha_i}}{|\mathbf{k}_{\alpha_i}|c}\int d^3k_{\alpha_f}\mathbf{k}^2_{\gamma_f}dk_{\gamma_f}\left(\frac{\mathbf{k}^2_{\beta_f}dk_{\beta_f}}{dS}\right)\delta(E_{\alpha_f}+E_{\beta_f} +E_{\gamma_f}-e_d-E_{\alpha_i})\,\delta(\mathbf{k}_{\alpha_f}+\mathbf{k}_{\beta_f}+\mathbf{k}_{\gamma_f}-\mathbf{k}_{\alpha_i}). \tag{13b}$$

Here, E_{α_i} and E_{α_f} are kinetic energies, defined correspondingly to E_{β_f} and E_{γ_f}; $(2\pi\hbar)^{-3}|\mathbf{k}_{\alpha_i}|c/k^0_{\alpha_i}$ is the incoming flux in the lab system; the energy factors contained in $\langle f|\mathcal{M}|i\rangle$ of Eq. (8b) and in $d\,\mathrm{Lips}(k_{\alpha_i}+k_d,k_{\alpha_f},k_{\beta_f},k_{\gamma_f})$ of Eq. (11) cancel exactly, once both are assumed to be computed in the same frame. The cross section (13a) is still spin dependent.

The spin-averaged fivefold differential cross section is

$$\frac{\overline{d^5\sigma}}{dSd^2\hat{\mathbf{k}}_{\beta_f}d^2\hat{\mathbf{k}}_{\gamma_f}}=\frac{1}{6}\sum_{M_{I_i}m_{s_i}}\sum_{m_{s_{\alpha_f}}m_{s_{\beta_f}}m_{s_{\gamma_f}}}\frac{d^5\sigma_{i\to f}}{dSd^2\hat{\mathbf{k}}_{\beta_f}d^2\hat{\mathbf{k}}_{\gamma_f}} =\frac{1}{6}\mathrm{Tr}[M(E_i\mathbf{p}_f\mathbf{q}_f)M^\dagger(E_i\mathbf{p}_f\mathbf{q}_f)]\ \ \mathrm{fps}. \tag{14}$$

In the figures the spin-averaged fivefold differential cross section is denoted by $d^5\sigma/dSd\Omega_1d\Omega_2$, the traditional notation.

The spin dependence of the initially prepared states is described by the Hermitian density matrix ρ_i, normalized to $\mathrm{Tr}\,\rho_i=1$. The density matrix ρ_i of the initially prepared states is the tensor product of density matrices for the nucleon and the deuteron, ρ^n and ρ^d, i.e.,

$$\rho_i=\rho^n\otimes\rho^d. \tag{15}$$

Their individual spin dependence is carried by the spin-$\frac{1}{2}$ operators S^{a_2} and the spin-1 operators S^{a_3}, defined in Sec. 3.2 of paper II. As in paper II, the set of product operators $\{S^{a_i}\}=\{S^{a_2}\otimes S^{a_3}\}$ is formed. They are normalized by

$$\mathrm{Tr}[S^{a_i}S^{b_i}]=6\,\delta_{a_ib_i}. \tag{16}$$

With those product operators S^{a_i} the initial density matrix gets the concise form

$$\rho_i=\frac{1}{6}\sum_{a_i}\mathrm{Tr}[\rho_iS^{a_i}]S^{a_i}. \tag{17}$$

The final-state polarization measurement is described by the projection operator ρ_f, i.e., $\rho_f^2=\rho_f$, which is the tensor product of corresponding projection operators for the three nucleons, i.e.,

$$\rho_f=N_f\rho^n\otimes\rho^n\otimes\rho^n, \tag{18}$$

with $N_f=2^{3-\mathcal{N}}$, $\mathcal{N}$ being the number of polarization measurements. ρ_f is normalized to $\mathrm{Tr}\,\rho_f=N_f$. Equation (18) corrects the imprecise description of this point in paper II. The operators ρ^n are parametrized in the form of the nucleon density matrix. Their individual spin dependence is carried

by the spin-$\frac{1}{2}$ operators S^{a_2}. The set of product operators $\{S^{a_f}\}=\{S^{a_2}\otimes S^{a_2}\otimes S^{a_2}\}$ is formed, which are normalized by

$$\mathrm{Tr}[S^{a_f}S^{b_f}]=8\,\delta_{a_f b_f}. \tag{19}$$

With these product operators S^{a_f} the projection operator ρ_f gets the concise form

$$\rho_f=\frac{1}{8}\sum_{a_f}\mathrm{Tr}[\rho_f S^{a_f}]S^{a_f}. \tag{20}$$

In terms of the scattering amplitude $M(E_i\mathbf{p}_f\mathbf{q}_f)$, of the initial density matrix ρ_i and of the final-state projection operator ρ_f, the spin-dependent differential cross section becomes

$$\frac{d^5\sigma}{dSd^2\hat{\mathbf{k}}_{\beta_f}d^2\hat{\mathbf{k}}_{\gamma_f}}=\mathrm{Tr}[M(E_i\mathbf{p}_f\mathbf{q}_f)\rho_i M^\dagger(E_i\mathbf{p}_f\mathbf{q}_f)\rho_f]\ \ \text{fps}. \tag{21}$$

Using the spin-averaged differential cross section $\overline{d^5\sigma/dSd^2\hat{\mathbf{k}}_{\beta_f}d^2\hat{\mathbf{k}}_{\gamma_f}}$ of Eq. (14) and the expansions (17) and (20) for the initial density matrix ρ_i and the final-state projection operator ρ_f, the spin-dependent differential cross sections take the form

$$\frac{d^5\sigma}{dSd^2\hat{\mathbf{k}}_{\beta_f}d^2\hat{\mathbf{k}}_{\gamma_f}}=\overline{\frac{d^5\sigma}{dSd^2\hat{\mathbf{k}}_{\beta_f}d^2\hat{\mathbf{k}}_{\gamma_f}}}\frac{1}{8}\sum_{a_i a_f}\mathrm{Tr}[\rho_i S^{a_i}]\mathrm{Tr}[\rho_f S^{a_f}]\frac{\mathrm{Tr}[M(E_i\mathbf{p}_f\mathbf{q}_f)S^{a_i}M^\dagger(E_i\mathbf{p}_f\mathbf{q}_f)S^{a_f}]}{\mathrm{Tr}[M(E_i\mathbf{p}_f\mathbf{q}_f)M^\dagger(E_i\mathbf{p}_f\mathbf{q}_f)]}. \tag{22}$$

Characteristic for the experimental setup of the studied reaction are the parameters in the initial density matrix ρ_i and in the final-state projection operator ρ_f which determine the expansion coefficient $\mathrm{Tr}[\rho_i S^{a_i}]\mathrm{Tr}[\rho_f S^{a_f}]$ in Eq. (22). Characteristic for the spin dependence of the reaction mechanism is the way in which the spin operators S^{a_i} of ρ_i and S^{a_f} of ρ_f weigh the spin matrix elements of the scattering amplitude. The experiment therefore aims at determining observables of the type $\mathrm{Tr}[M(E_i\mathbf{p}_f\mathbf{q}_f)S^{a_i}M^\dagger(E_i\mathbf{p}_f\mathbf{q}_f)S^{b_f}]/\mathrm{Tr}[M(E_i\mathbf{p}_f\mathbf{q}_f)M^\dagger(E_i\mathbf{p}_f\mathbf{q}_f)]$. A particular choice of the spin operators S^{a_i} and S^{b_f} defines particular spin observables; their notation is standardized in Ref. [8].

E. Problem in the comparison of theoretical predictions and experimental data

The experimental setup for breakup usually works with two particle detectors at two fixed angles measuring $\hat{\mathbf{k}}_{\beta_f}$ and $\hat{\mathbf{k}}_{\gamma_f}$ and determines cross sections as functions of the arclength S on the kinematical curve corresponding to the two kinetic energies E_{β_f} and E_{γ_f}. A sound comparison requires the same kinematical curve for the experimental interpretation of data and for the theoretical prediction. However, the experimental interpretation of data usually prefers relativistic kinematics, whereas theory prefers nonrelativistic kinematics, since the description of dynamics is nonrelativistic anyhow. Without a relativistic treatment of the dynamics there is no fully consistent description of the experimental data and of the theoretical prediction. Thus, approximative identification procedures have to be applied; a discussion of this point and a suggestion for identification is given in Ref. [9]. We follow a somehow different procedure. At the rather low energies considered in this paper the resulting kinematical curves, defined in Eq. (12), are often quite similar for relativistic and nonrelativistic kinematics, but there are special situations with dramatic differences. Figures 1 and 2 give examples for either case at 65 MeV nucleon lab energy and at 52 MeV deuteron lab energy, respectively.

Figure 1 refers to the space star configuration at 65 MeV nucleon lab energy, which is realized for relativistic and nonrelativistic kinematics at slightly different scattering angles. There are only minor differences between the relativistic and nonrelativistic kinematical curves corresponding to the same angles. However, the kinematical curves for slightly different angles corresponding to the exact space star configuration with relativistic and nonrelativistic kinematics are even almost identical. The right-hand side of Fig. 1 shows a sample effect on observables, which arises from differences in the kinematical curves. Correspondence is obtained by scaling all considered kinematical curves to the length of the relativistic arclength. The length of the kinematical curves before scaling is recorded in the figure caption; the discrepancy between the results of different identification procedures is small.

The example of Fig. 2 is more dramatic. It refers to the quasi-free-scattering (QFS) configuration for 52 MeV deuteron lab energy. Again, this special situation is with relativistic and nonrelativistic kinematics realized only for slightly different scattering angles. However, in this case there are quite large differences between the relativistic and nonrelativistic kinematical curves corresponding to the same angles; the reason is that the critical situation $(42.26°,42.26°,180.0°)$, at which the relativistic locus collapses to a point, is near and that in nonrelativistic kinematics that critical situation occurs at larger angles. In contrast, the kinematical curves for slightly different angles corre sponding to the exact QFS configuration with relativistic and nonrelativistic kinematics are quite close. The right-hand side of Fig. 1 shows a sample effect on observables, which

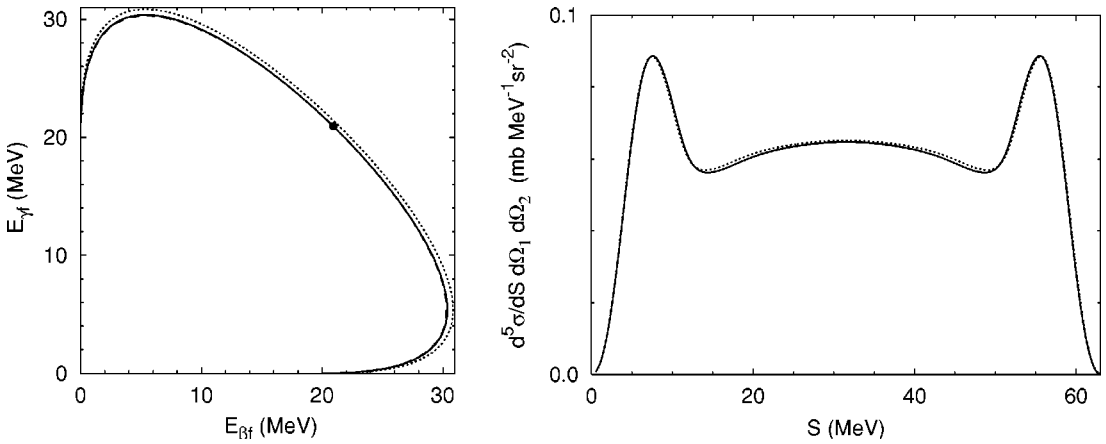

FIG. 1. Left side: kinematical curves for the relativistic space star configuration (53.5°,53.5°,120.0°) with relativistic (dashed curve) and nonrelativistic (dotted curve) kinematics and for the nonrelativistic space star configuration (54.0°,54.0°,120.0°) with nonrelativistic kinematics (solid curve) at 65 MeV nucleon lab energy. The total arclengths are 62.92, 63.64, and 63.04 MeV, respectively. The solid and dashed curves are almost indistinguishable in the plot. The dot indicates the position of the exact space star point. Right side: differential cross section as a function of the arclength S along the kinematical curve for the space star configurations of nucleon-deuteron breakup at 65 MeV nucleon lab energy. As in all calculations of this paper, the results are obtained with a nonrelativistic arclength S. Results for the nonrelativistic space star configuration (54.0°,54.0°,120.0°) (solid curve) and for the relativistic space star configuration (53.5°,53.5°,120.0°) (dotted curve) are compared.

arises from differences in the kinematical curves. Correspondence is naturally achieved wihout scaling, since the experimental data at this energy are given and will be given as functions of $S/S_{\max}$, $S_{\max}$ being the full arclength of the relativistic kinematical curve; we follow that procedure. The respective length of the kinematical curves is recorded in the figure caption. The sensitivity on the chosen kinematical curve is alarmingly large. This observation also implies that the corrections arising from finite geometry can become sizable in this kinematical configuration.

With respect to the experimental data that this paper attempts to describe or to predict, we therefore use the following theoretical strategy. We employ nonrelativistic kinematics throughout, i.e., we use the lab cross section as given in Eq. (13a), define the arclength S with nonrelativistic energies, and use the nonrelativistic phase space factor

$$\begin{aligned}\mathrm{fps} = (2\pi)^4 \hbar^2 \frac{m_N}{|\mathbf{k}_{\alpha_i}|} \int d^3k_{\alpha_f} \mathbf{k}_{\gamma_f}^2 dk_{\gamma_f} \left(\frac{\mathbf{k}_{\beta_f}^2 dk_{\beta_f}}{dS} \right) \\ \times \delta\left(\frac{\mathbf{k}_{\alpha_f}^2}{2m_N} + \frac{\mathbf{k}_{\beta_f}^2}{2m_N} + \frac{\mathbf{k}_{\gamma_f}^2}{2m_N} - e_d - \frac{\mathbf{k}_{\alpha_i}^2}{2m_N} \right) \\ \times \delta(\mathbf{k}_{\alpha_f} + \mathbf{k}_{\beta_f} + \mathbf{k}_{\gamma_f} - \mathbf{k}_{\alpha_i}). \end{aligned} \tag{23}$$

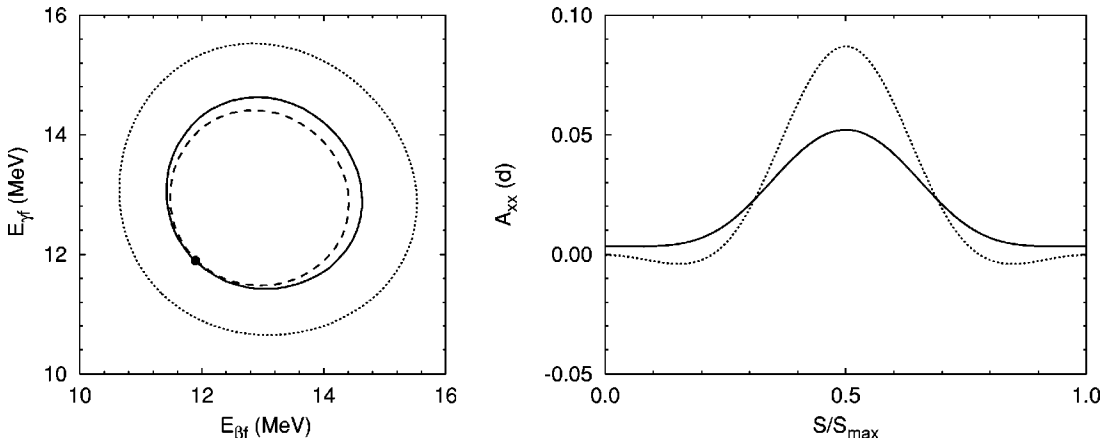

FIG. 2. Left side: kinematical curves for the relativistic QFS configuration (42.16°,42.16°,180.0°) with relativistic (dashed curve) and nonrelativistic (dotted curve) kinematics and for nonrelativistic QFS configuration (42.32°,42.32°,180.0°) with nonrelativistic kinematics (solid curve) at 52 MeV deuteron lab energy. Total arclengths are 9.22, 15.34, and 10.09 MeV, respectively. The dot indicates the position of the exact QFS point. Right side: deuteron tensor analyzing power $A_{xx}(d)$ as a function of the fractional arclength $S/S_{\max}$ along the kinematical curve for QFS configurations of nucleon-deuteron breakup at 52 MeV deuteron lab energy. As in all calculations of this paper, the results are obtained with a nonrelativistic arclength S. Results for nonrelativistic QFS configuration (42.32°,42.32°,180.0°) (solid curve) and for relativistic QFS configuration (42.16°,42.16°,180.0°) (dotted curve) are compared.

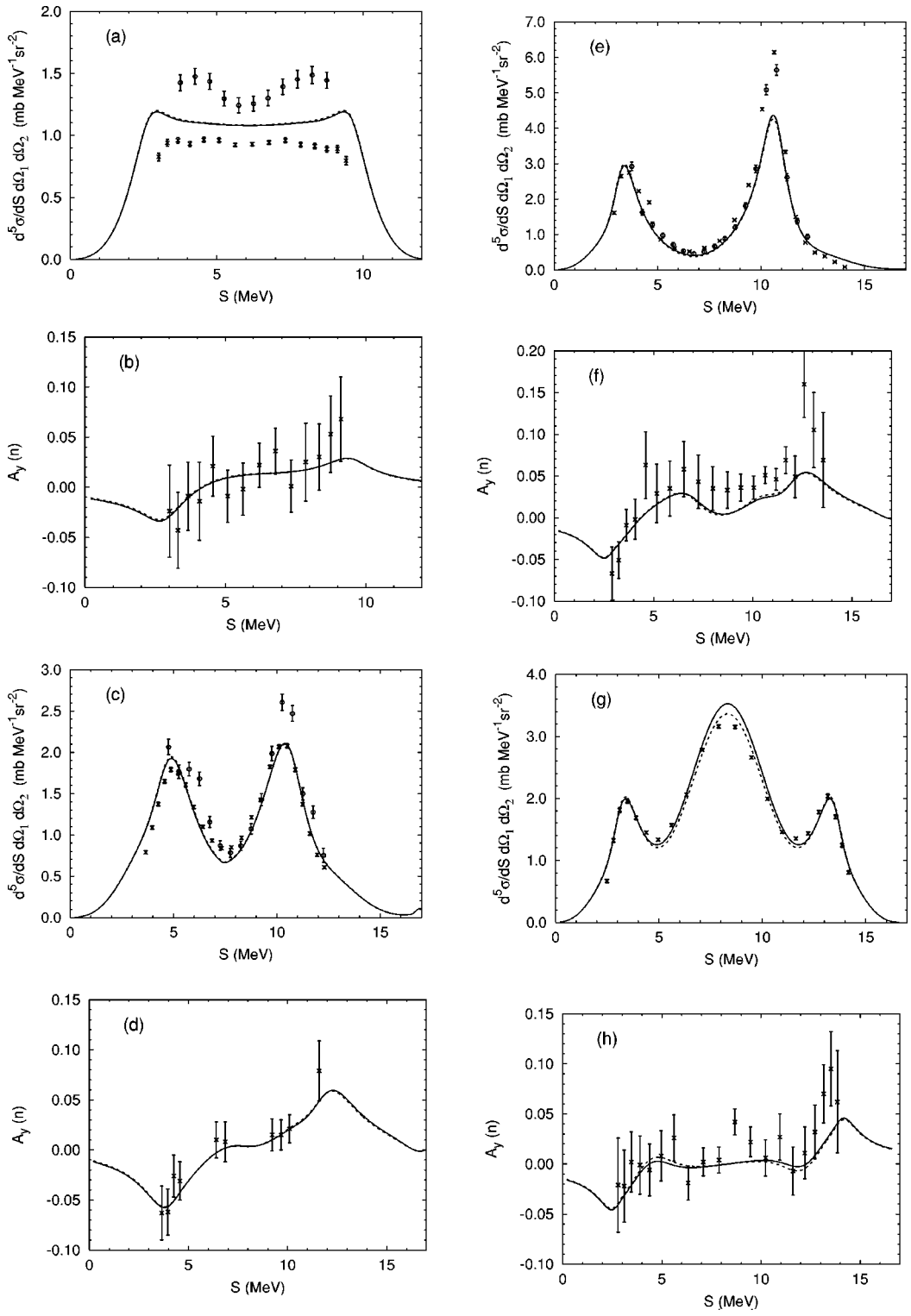

FIG. 3. Differential cross section and nucleon analyzing power $A_y(n)$ as functions of the arclength S along the kinematical curve for various configurations of nucleon-deuteron breakup at 13 MeV nucleon lab energy. (a),(b) space star configuration (50.5°,50.5°,120.0°), (c),(d) collinearity configuration (50.5°,62.5°,180.0°), (e),(f) FSI configuration (39.0°,62.5°,180.0°), and (g),(h) QFS configuration (39.0°,39.0°,180.0°). Results of the coupled-channel potential with Δ-isobar excitation (solid curve) are compared with results of the Paris potential (dashed curve). The experimental data are from Ref. [10] referring to neutron-deuteron scattering (circles) and from Ref. [11] referring to proton-deuteron scattering (crosses).

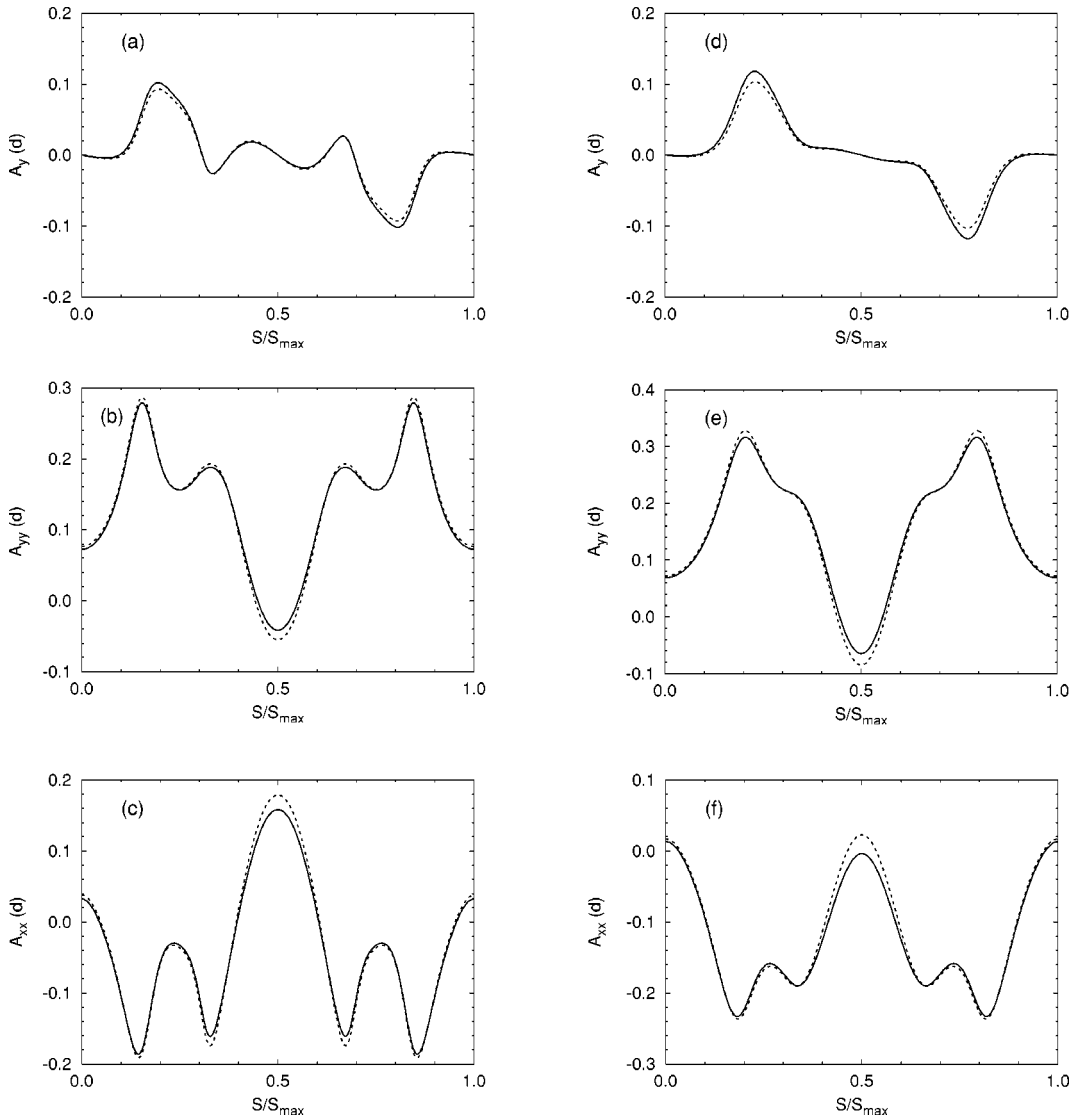

FIG. 4. Deuteron analyzing powers $A_y(d)$, $A_{yy}(d)$, and $A_{xx}(d)$ as functions of the fractional arclength $S/S_{\max}$ along the kinematical curve for various configurations of nucleon-deuteron breakup at 52 MeV deuteron lab energy. (a)–(c) configuration (32.5°,32.5°,180.0°) and (d)–(f) configuration (37.0°,37.0°,180.0°). Results of the coupled-channel potential with Δ-isobar excitation (solid curve) are compared with results of the Paris potential (dashed curve). Since the experimental analysis uses an arclength S based on relativistic kinematics, the theoretical nonrelativistic description resorts to the identification procedure of Sec. II E. The following scattering angles were used for the calculation (the ratio of the total relativistic over nonrelativistic arclengths is given simultaneously in square brackets): (a)–(c) (32.7°,32.7°,180.0°)[1.002] and (d)–(f) (37.2°,37.2°,180.0°)[1.002].

We also note that the fit of the underlying baryonic potentials to data is based on a corresponding entirely nonrelativistic phase space factor. Thus, internal consistency requires the use of the nonrelativistic phase space factor (23). Furthermore, that form of description is natural for experimental data that are derived from a nonrelativistic analysis. If, however, the analysis of experimental data is relativistic, we meet the chosen particular kinematic configurations of the experiment, such as space star, collinearity, final-state interaction (FSI), or QFS in nonrelativistic kinematics only by an appropriate change of scattering angles, thereby approximating the relativistic kinematical curves nonrelativistically and scaling the resulting arclengths to the value of the relativistic length. In case the experimental data do not refer to a particular kinematic configuration, we still change the scattering angles slightly till the agreement of relativistic and nonrelativistic kinematical curves is significantly improved.

III. RESULTS

Observables of breakup in nucleon-deuteron scattering are calculated for 13 MeV and 65 MeV nucleon lab energy and for 52 MeV deuteron lab energy. The calculations are based on the coupled-channel two-baryon potential $A2$, defined in Ref. [2]; it allows for single Δ-isobar excitation. Its nucleonic reference potential, being almost phase equivalent to $A2$ at low energies, is the Paris potential [7]. Both potentials are

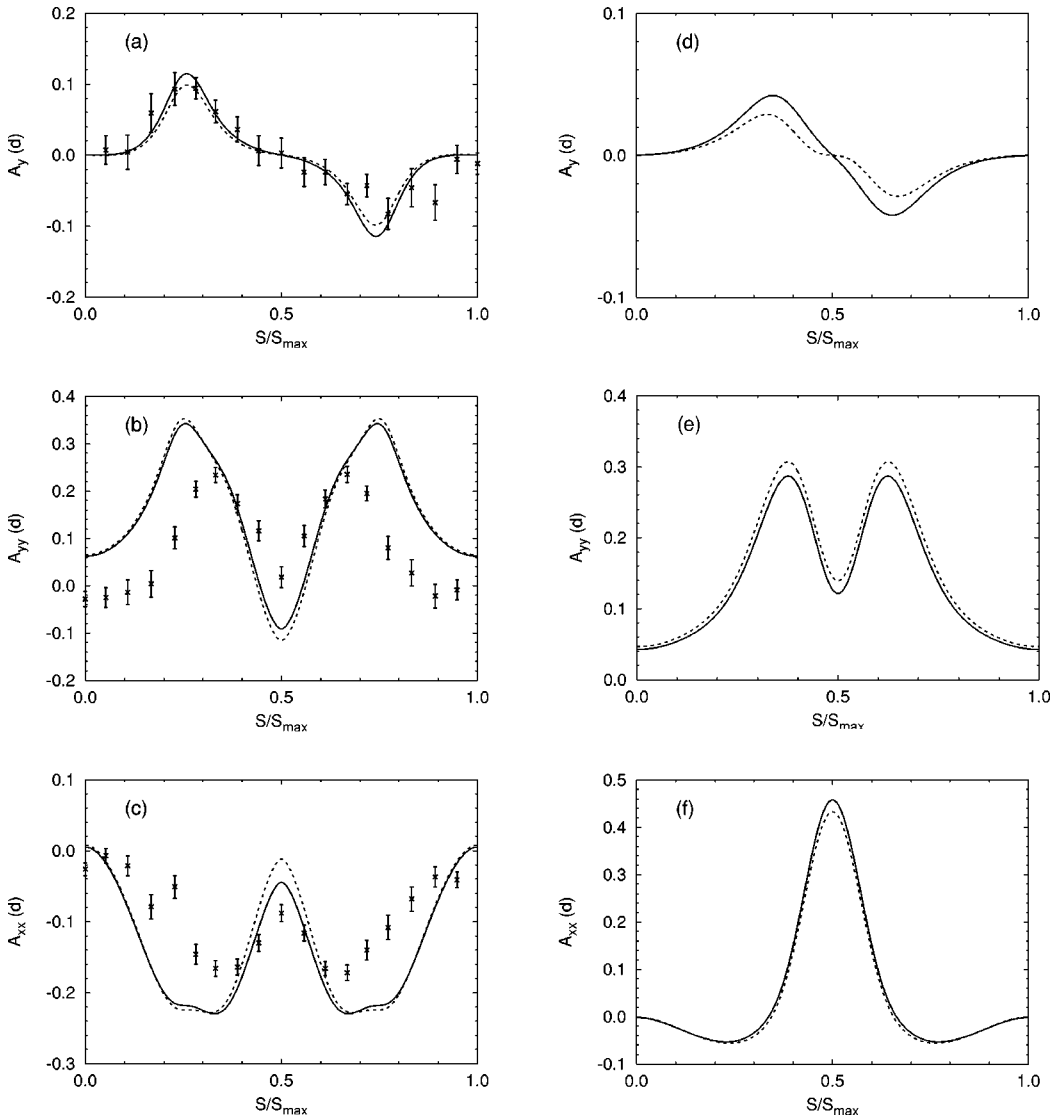

FIG. 5. Deuteron analyzing powers $A_y(d)$, $A_{yy}(d)$, and $A_{xx}(d)$ as functions of the fractional arclength $S/S_{\max}$ along the kinematical curve for various configurations of nucleon-deuteron breakup at 52 MeV deuteron lab energy. (a)–(c) configuration (38.7°,38.7°,180.0°) and (d)–(f) configuration (41.0°,41.0°,180.0°). Results of the coupled-channel potential with Δ-isobar excitation (solid curve) are compared with results of the Paris potential (dashed curve). The experimental data are from Ref. [13] and refer to proton-deuteron scattering; they are given there as functions of the arclength S measured clockwise along the kinematical curve. The $A_y(d)$ data are therefore readjusted to match our convention of a counterclockwise S. Furthermore, since the experimental analysis uses an arclength S based on relativistic kinematics, the theoretical nonrelativistic description resorts to the identification procedure of Sec. II E. The following scattering angles were used for the calculation (the ratio of the total relativistic over nonrelativistic arclengths is given simultaneously in square brackets): (a)–(c) (38.9°,38.9°,180.0°)[1.004] and (d)–(f) (41.2°,41.2°,180.0°)[1.002].

used in order to maintain consistency with papers I and II. Both potentials are taken into account in partial waves up to two-baryon total angular momentum $I=4$. Channel coupling to the Δ isobar is considered in all isospin triplet partial waves up to $I=2$. The symmetrized breakup transition matrix $\langle \phi_0(\mathbf{p}_f\mathbf{q}_f)\nu_0(m_f)|U_0(E_i+i0)|\phi_\alpha(\mathbf{q}_i)\nu_{\alpha_i}\rangle$ to be calculated is expanded into three-body partial waves; the expansion is terminated at the three-body total angular momentum $\mathcal{J}=\frac{27}{2}$. Any additional three-body partial wave $\mathcal{J}$ yields changes not visible in plots.

The calculations are done without Coulomb interaction between protons, they therefore refer to neutron-deuteron breakup. Nevertheless, results are freely compared to proton-deuteron experiments. Kinematic regions, in which both protons in the final state have small relative momenta and which therefore could see the Coulomb repulsion between the protons, do not occur in the presented plots.

Results for spin-averaged and spin-dependent observables at 13 MeV nucleon lab energy are given in Fig. 3. The experimental data appear analyzed in Refs. [10,11] nonrelativistically. The theoretical predictions of this paper do not need any readjustment of the nonrelativistic kinematical curves for a sound comparison. Anyhow, at this energy the difference between the relativistic and the nonrelativistic kinemati-

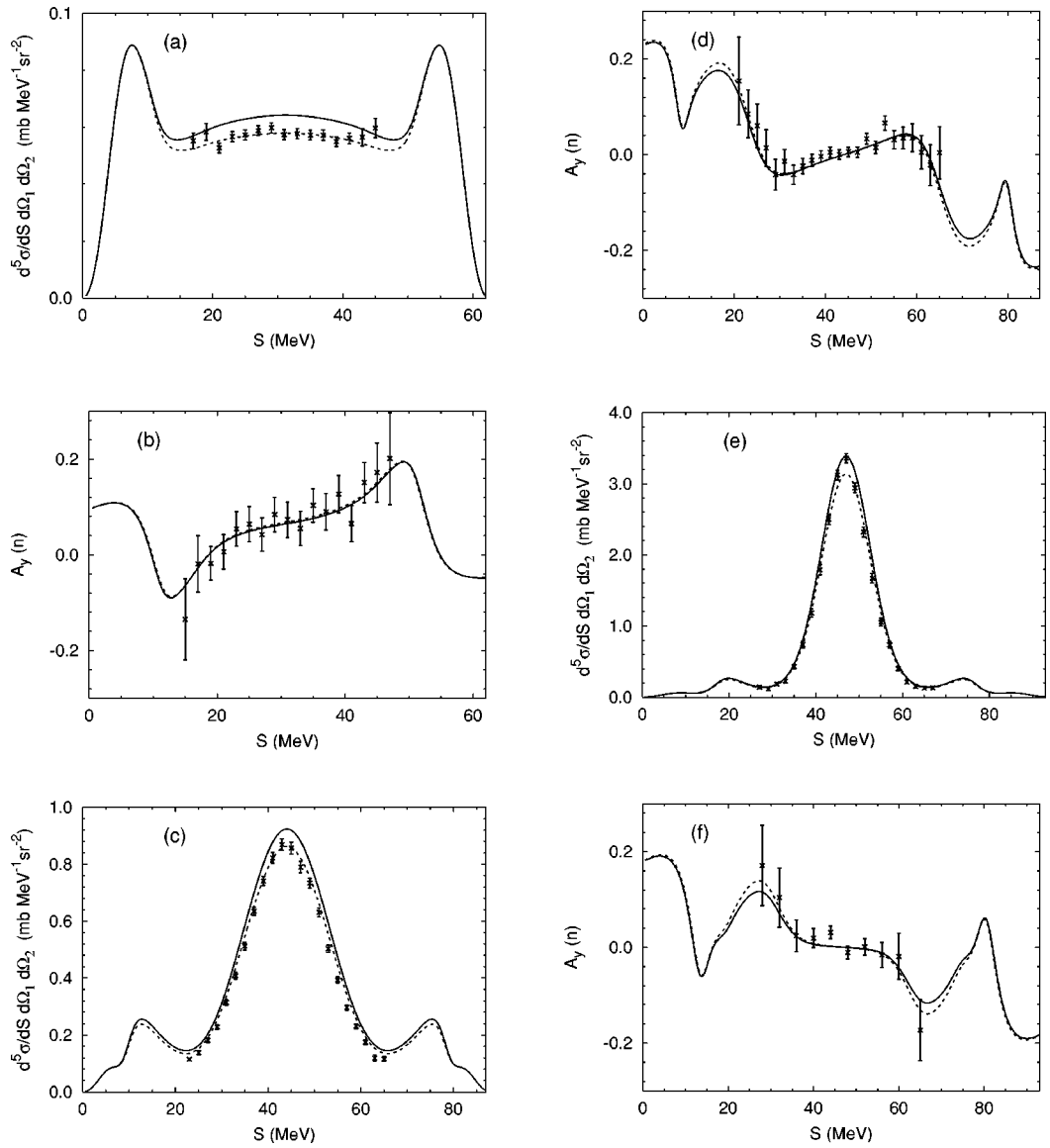

FIG. 6. Differential cross section and nucleon analyzing power $A_y(n)$ as functions of the arclength S along the kinematical curve for various configurations of nucleon-deuteron breakup at 65 MeV nucleon lab energy. (a),(b) space star configuration (54.0°,54.0°,120.0°), (c),(d) coplanar star configuration (35.2°,35.2°,180.0°), and (e),(f) QFS configuration (44.0°,44.0°,180.0°). Results of the coupled-channel potential with Δ-isobar excitation (solid curve) are compared with results of the Paris potential (dashed curve). The experimental data are from Refs. [15,16] and refer to proton-deuteron scattering. Since the experimental analysis uses an arclength S based on relativistic kinematics, the theoretical nonrelativistic description has to resort to the identification procedure of Sec. II E. The following scattering angles were used for the calculation (the ratio of the total relativistic over nonrelativistic arclengths is given simultaneously in square brackets): (a),(b) (54.5°,54.5°,120.0°)[0.999], (c),(d) (35.5°,35.5°,180.0°)[0.999], and (e),(f) (44.5°,44.5°,180.0°)[0.997].

cal curves is extremely small. The disagreement between the theoretical predictions and the experimental data is most striking for the differential cross section in the space star configuration of Fig. 3(a). The experimental data for proton-deuteron and neutron-deuteron breakup are surprisingly far apart. Neither data set is accounted for by theory as has been already observed by others [5]. Furthermore, the calculations are unable to reproduce the height of the differential cross section peaks at arclength S around 10 MeV in the collinearity and in the FSI configurations of Figs. 3(c) and 3(e). This fact is a particular feature of the chosen potentials; additional calculations with more modern potentials are able to remove that discrepancy [12]. In the studied observables the effect of the Δ isobar and of its mediated three-nucleon force is irrelevant; there is a mild, but nonbeneficial, effect on the central peak of the differential cross section in the QFS configuration of Fig. 3(g).

Results for deuteron analyzing powers of deuteron-proton scattering at 52 MeV deuteron lab energy are given in Figs. 4 and 5. The experimental data in Figs. 5(a)–5(c) are from Ref. [13]. There exist also new, but still preliminary, experimental data [14] for all observables of Figs. 4 and 5. The agreement between our theoretical predictions and these new data appears by and large satisfactory. The new data are not ready-

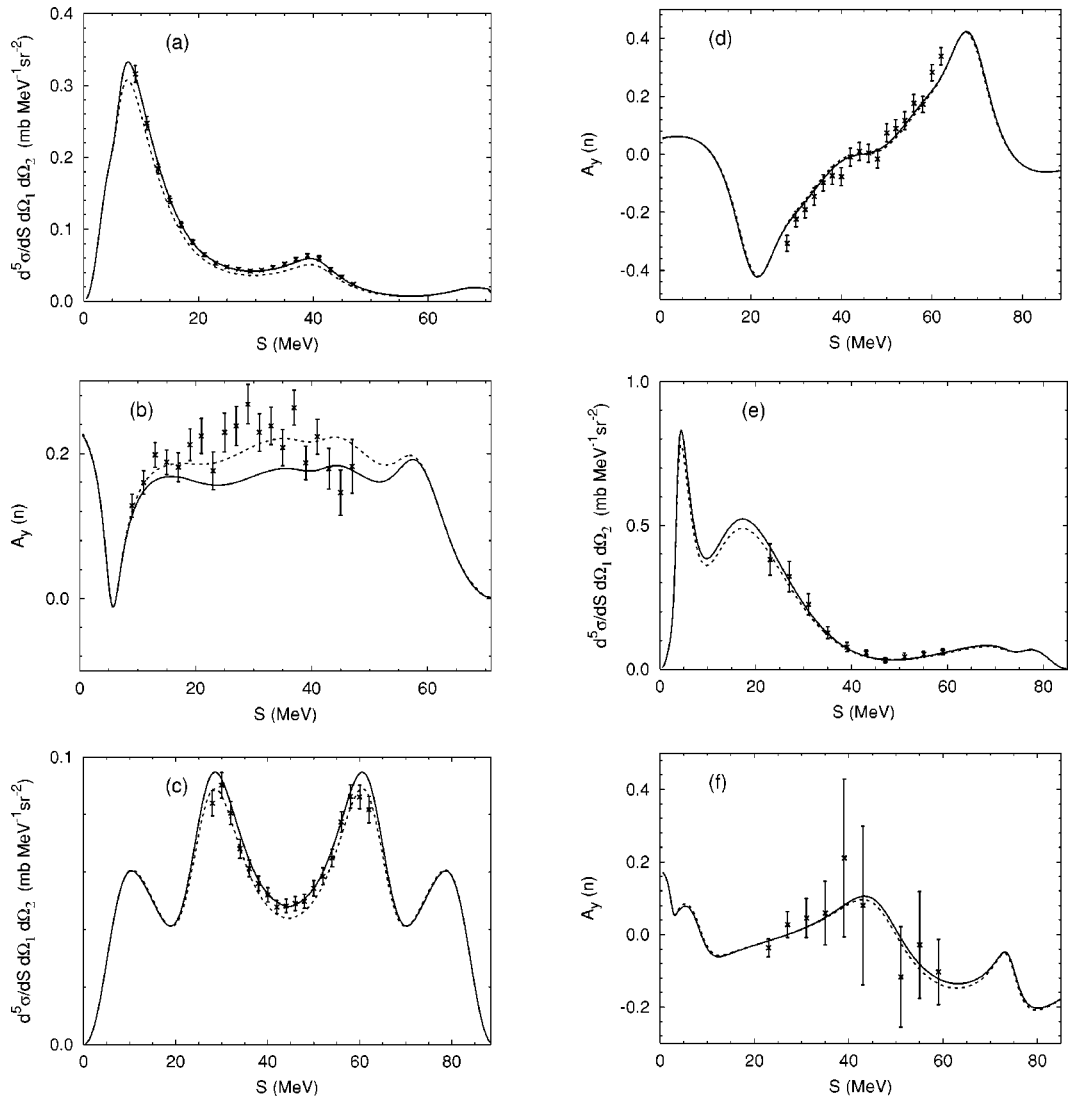

FIG. 7. Differential cross section and nucleon analyzing power $A_y(n)$ as functions of the arclength S along the kinematical curve for various configurations of nucleon-deuteron breakup at 65 MeV nucleon lab energy. (a),(b) collinear configuration (30.0°,98.0°,180.0°), (c),(d) collinear configuration (59.5°,59.5°,180.0°), and (e),(f) nonspecific configuration (20.0°,45.0°,180.0°). Results of the coupled-channel potential with Δ-isobar excitation (solid curve) are compared with results of the Paris potential (dashed curve). The experimental data are from Refs. [9,17] and refer to proton-deuteron scattering. Since the experimental analysis uses an arclength S based on relativistic kinematics, the theoretical nonrelativistic description has to resort to the identification procedure of Sec. II E. The following scattering angles were used for the calculation (the ratio of the total relativistic over nonrelativistic arclengths is given simultaneously in square brackets): (a),(b) (30.3°,98.9°,180.0°)[1.000], (c),(d) (60.0°,60.0°,180.0°)[0.993], and (e),(f) (20.2°,45.5°,180.0°)[0.999].

yet for publication; our predictions are given for further reference. The experimental data of Refs. [13,14] are and will be analyzed with relativistic kinematics; the identification procedure described in Sec. II E is used. As discussed there, data and results for the configuration (41.0°,41.0°,180.0°) are most affected. On the other hand, the Δ-isobar effects on the considered observables remain small.

Results for spin-averaged and spin-dependent observables at 65 MeV nucleon lab energy are given in Figs. 6 and 7. All experimental data refer to proton-deuteron scattering. The experimental setup realizes the particular scattering configurations such as space star, coplanar star, QFS, and collinearity within nonrelativistic kinematics. In contrast, the arclength S employed for presenting data is derived from relativistic kinematics; thus, the identification procedure for the arclength described in Sec. II E has to be used. The agreement between theoretical predictions and experimental data is satisfactory. The effects of the Δ isobar and of its mediated three-nucleon force become more noticeable in some observables, e.g., for the differential cross section in space star and collinear configurations. For some other observables, e.g., for the differential cross section in coplanar star and QFS configurations, the total Δ-isobar effects are dominated by the dispersive two-body effect; that aspect is worrisome and needs further investigation. The Δ-isobar effects are not always beneficial.

IV. CONCLUSIONS

The main purpose of the paper is the presentation of our technique for calculating breakup observables in nucleon-deuteron scattering; the paper also gives sample physics results. In order to preserve continuity with our previous papers I and II on elastic nucleon-deuteron scattering, the same two-baryon potentials are used as dynamic basis. In the light of existing improved two-nucleon potentials, the employed potentials are outdated; however, we believe that the theoretical predictions will only be affected in details.

The highlight of a theoretical prediction is reached when it is technically reliable, but fails in accounting for data. That situation occurs in elastic nucleon-deuteron scattering with the neutron analyzing power at low energies and with the Sagara discrepancy in the minima of the differential cross section at higher energies. Whereas the latter discrepancy is removed by a three-nucleon force [6], the disagreement for the low-energy neutron analyzing power, strongly dependent on the two-nucleon interaction in P waves, remains a puzzle. Observables of nucleon-deuteron breakup are studied with the same motivation of finding disagreements through which one may be able to learn more about two-nucleon and three-nucleon forces. Though some disagreement between theoretical predictions and experimental data is found in instances, a clear-cut discrepancy for a theoretical description without a three-nucleon force is not seen yet. But the search is still on.

ACKNOWLEDGMENTS

The authors thank Colston Chandler for pointing out early references on the product integration method; they also thank Juerg Jourdan and Ingo Sick for a discussion of experimental data. A.D. acknowledges a valuable DAAD grant for graduate studies at the University of Hannover. The numerical calculations were performed at Regionales Rechenzentrum für Niedersachsen.

APPENDIX: TECHNICAL DETAILS OF THE CALCULATION

The solution of the integral equation (7) for the half-shell transition matrix $\langle \mathbf{g}_\alpha | G_0(Z)U(Z)G_0(Z)|\mathbf{g}_\alpha\rangle$ with $Z=E_i+i0$ is the numerical basis for determining the breakup S matrix (4). The quantities in Eq. (7) are operators with respect to the spectator momentum $\mathbf{q}$ and matrices with respect to the rank labels determining the form factor states $|\mathbf{g}_\alpha\rangle$ and $\langle \mathbf{g}_\alpha|$ and the discrete quantum numbers. The integral equation (7) is solved in the nonorthogonal basis $|iq\chi(Ij)\Pi\mathcal{J}\mathcal{M}_\mathcal{J}\mathcal{T}\mathcal{M}_\mathcal{T}\rangle_\alpha$ of paper II, i.e.,

$$|iq\chi(Ij)\Pi\mathcal{J}\mathcal{M}_\mathcal{J}\mathcal{T}\mathcal{M}_\mathcal{T}\rangle_\alpha=\sum_{M_I m_j}\sum_{M_T m_t}|g_\alpha^{(i\pi IT)}M_I M_T\rangle|q(ls)jm_j tm_t b\rangle_\alpha\langle IM_I jm_j|\mathcal{J}\mathcal{M}_\mathcal{J}\rangle\langle TM_T tm_t|\mathcal{T}\mathcal{M}_\mathcal{T}\rangle, \tag{A1a}$$

$$|iq\chi(Ij)\Pi\mathcal{J}\mathcal{M}_\mathcal{J}\mathcal{T}\mathcal{M}_\mathcal{T}\rangle_\alpha=\sum_{LSB}\int p^2dp|pq[(LS)I(ls)j]\mathcal{J}\mathcal{M}_\mathcal{J}(Tt)\mathcal{T}\mathcal{M}_\mathcal{T}Bb\rangle_\alpha\langle pLSB|g_\alpha^{(i\pi IT)}\rangle, \tag{A1b}$$

and for the initial nucleon-deuteron state (6) which can be expanded in terms of those basis states, i.e.,

$$\begin{aligned}|\phi_\alpha(\mathbf{q}_i)\nu_{\alpha_i}\rangle=G_0(E_i+i0)\sum_{\Pi\mathcal{J}\mathcal{M}_\mathcal{J}\mathcal{T}M_\mathcal{T}}\sum_{l_i m_{l_i} j_i m_{j_i}}&|i_0q_i\chi_i(I_0j_i)\Pi\mathcal{J}\mathcal{M}_\mathcal{J}\mathcal{T}\mathcal{M}_\mathcal{T}\rangle_\alpha\langle I_0M_{I_i}j_i m_{j_i}|\mathcal{J}\mathcal{M}_\mathcal{J}\rangle\langle l_i m_{l_i}s_0m_{s_i}|j_i m_{j_i}\rangle Y^*_{l_i m_{l_i}}(\hat{q}_i)\\ &\times\langle T_0M_{T_0}t_0m_{t_0}|\mathcal{T}\mathcal{M}_\mathcal{T}\rangle.\end{aligned} \tag{A2a}$$

Thus, the matrix elements ${}_\alpha\langle i'q'\chi'(I'j')\Pi\mathcal{J}\mathcal{M}_\mathcal{J}\mathcal{T}\mathcal{M}_\mathcal{T}|G_0(E_i+i0)U(E_i+i0)G_0(E_i+i0)|i_0q_i\chi_i(I_0j_i)\Pi\mathcal{J}\mathcal{M}_\mathcal{J}\mathcal{T}\mathcal{M}_\mathcal{T}\rangle_\alpha$ are to be calculated according to

$$\begin{aligned}&{}_\alpha\langle i'q'\chi'(I'j')\Pi\mathcal{J}\mathcal{M}_\mathcal{J}\mathcal{T}\mathcal{M}_\mathcal{T}|G_0(E_i+i0)U(E_i+i0)G_0(E_i+i0)|i_0q_i\chi_i(I_0j_i)\Pi\mathcal{J}\mathcal{M}_\mathcal{J}\mathcal{T}\mathcal{M}_\mathcal{T}\rangle_\alpha\\ &\quad={}_\alpha\langle i'q'\chi'(I'j')\Pi\mathcal{J}\mathcal{M}_\mathcal{J}\mathcal{T}\mathcal{M}_\mathcal{T}|PG_0(E_i+i0)|i_0q_i\chi_i(I_0j_i)\Pi\mathcal{J}\mathcal{M}_\mathcal{J}\mathcal{T}\mathcal{M}_\mathcal{T}\rangle_\alpha\\ &\qquad+\sum_{i''i_\chi}\int q^2dq_\alpha\langle i'q'\chi'(I'j')\Pi\mathcal{J}\mathcal{M}_\mathcal{J}\mathcal{T}\mathcal{M}_\mathcal{T}|PG_0(E_i+i0)|i''q\chi(Ij)\Pi\mathcal{J}\mathcal{M}_\mathcal{J}\mathcal{T}\mathcal{M}_\mathcal{T}\rangle_\alpha(i''|\mathbf{T}_\alpha(E_i+i0,q\chi(Ij))|i)\\ &\qquad\times{}_\alpha\langle iq\chi(Ij)\Pi\mathcal{J}\mathcal{M}_\mathcal{J}\mathcal{T}\mathcal{M}_\mathcal{T}|G_0(E_i+i0)U(E_i+i0)G_0(E_i+i0)|i_0q_i\chi_i(I_0j_i)\Pi\mathcal{J}\mathcal{M}_\mathcal{J}\mathcal{T}\mathcal{M}_\mathcal{T}\rangle_\alpha.\end{aligned} \tag{A2b}$$

The final breakup states $|\phi_0(\mathbf{p}_f\mathbf{q}_f)\nu_0(m_f)\rangle$ of Eqs. (3) are related to the three-particle basis states $|pq\nu(Ij)\rangle_\alpha$ of paper I by

$$|\phi_0(\mathbf{p}_f\mathbf{q}_f)\nu_0(m_f)\rangle = \sum_{\mathcal{J}\mathcal{M}_\mathcal{J}\mathcal{T}\mathcal{M}_\mathcal{T} L_f M_{L_f} S_f M_{S_f} I_f M_{I_f} T_f M_{T_f}} \sum_{l_f m_{l_f} j_f m_{j_f}} |p_f q_f[(L_f S_f) I_f (l_f s_\alpha) j_f]\mathcal{J}\mathcal{M}_\mathcal{J}(T_f t_\alpha)\mathcal{T}\mathcal{M}_\mathcal{T} Bb\rangle_\alpha$$
$$\times \langle I_f M_{I_f} j_f m_{j_f}|\mathcal{J}\mathcal{M}_\mathcal{J}\rangle \langle L_f M_{L_f} S_f M_{S_f}|I_f M_{I_f}\rangle Y^*_{L_f M_{L_f}}(\hat{p}_f) \langle s_\beta m_{s_{\beta_f}} s_\gamma m_{s_{\gamma_f}}|S_f M_{S_f}\rangle$$
$$\times \langle l_f m_{l_f} s_\alpha m_{s_{\alpha_f}}|j_f m_{j_f}\rangle Y^*_{l_f m_{l_f}}(\hat{q}_f) \langle T_f M_{T_f} t_\alpha m_{t_{\alpha_f}}|\mathcal{T}\mathcal{M}_\mathcal{T}\rangle \langle t_\beta m_{t_{\beta_f}} t_\gamma m_{t_{\gamma_f}}|T_f M_{T_f}\rangle \sqrt{2}. \quad \text{(A3a)}$$

The factor $\sqrt{2}$ arises in Eq. (A3a), since the basis states $|pq\nu(Ij)\rangle_\alpha$ are antisymmetrized by $(1-P_{\beta\gamma})/2$ in the pair $(\beta\gamma)$. Thus, the on-shell breakup amplitude of Eq. (5b) has the following partial-wave projected form:

$$_\alpha\langle p_f q_f \nu'(I'j')|U_0(E_i+i0)|i_0 q_i \chi_i(I_0 j_i)\Pi\mathcal{J}\mathcal{M}_\mathcal{J}\mathcal{T}\mathcal{M}_\mathcal{T}\rangle_\alpha$$
$$= \sum_{i'' i_\chi} \int q^2 dq\, {}_\alpha\langle p_f q_f \nu'(I'j')|(1+P)|i'' q\chi(Ij)\Pi\mathcal{J}\mathcal{M}_\mathcal{J}\mathcal{T}\mathcal{M}_\mathcal{T}\rangle_\alpha (i''|\mathbf{T}_\alpha(E_i+i0,q\chi(Ij))|i)$$
$$\times {}_\alpha\langle iq\chi(Ij)\Pi\mathcal{J}\mathcal{M}_\mathcal{J}\mathcal{T}\mathcal{M}_\mathcal{T}|G_0(E_i+i0)U(E_i+i0)G_0(E_i+i0)|i_0 q_i\chi_i(I_0 j_i)\Pi\mathcal{J}\mathcal{M}_\mathcal{J}\mathcal{T}\mathcal{M}_\mathcal{T}\rangle_\alpha. \quad \text{(A3b)}$$

All matrix elements of Eqs. (A2b) and (A3b) are diagonal in the three-particle quantum numbers parity Π, total angular momentum $\mathcal{J}$, and its projection $\mathcal{M}_\mathcal{J}$ and total isospin $\mathcal{T}$ and its projection $\mathcal{M}_\mathcal{T}$. Furthermore, they are independent of the projections $\mathcal{M}_\mathcal{J}$ and $\mathcal{M}_\mathcal{T}$. In each partial wave $(\Pi\mathcal{J}\mathcal{M}_\mathcal{J}\mathcal{T}\mathcal{M}_\mathcal{T})$ they are only required for at most three initial states $|i_0 q_i \chi_i(I_0 j_i)\Pi\mathcal{J}\mathcal{M}_\mathcal{J}\mathcal{T}\mathcal{M}_\mathcal{T}\rangle_\alpha$, distinguished by $\chi_i(I_0 j_i)$, but for a full set of final states ${}_\alpha\langle i'q'\chi'(I'j')\Pi\mathcal{J}\mathcal{M}_\mathcal{J}\mathcal{T}\mathcal{M}_\mathcal{T}|$ in case of the transition matrix elements (A2b), and for the three-particle partial-wave states ${}_\alpha\langle p_f q_f \nu'(I'j')|$ in case of the breakup elements (A3b). The quadrature in Eq. (A3b) for the breakup amplitude can be carried out without technical problems. The solution of the integral equation (A2b) is more demanding. It is initiated by determining the first terms of the corresponding, usually nonconvergent, Neumann series up to a chosen order M iteratively and then constructing a converging approximation for the partial-wave projected solution ${}_\alpha\langle i'q'\chi'(I'j')|K(\lambda=1)|i_0 q_i\chi_i(I_0 j_i)\rangle_\alpha = {}_\alpha\langle i'q'\chi'(I'j')\Pi\mathcal{J}\mathcal{M}_\mathcal{J}\mathcal{T}\mathcal{M}_\mathcal{T}|G_0(E_i+i0)U(E_i+i0)G_0(E_i+i0)|i_0 q_i\chi_i(I_0 j_i)\Pi\mathcal{J}\mathcal{M}_\mathcal{J}\mathcal{T}\mathcal{M}_\mathcal{T}\rangle_\alpha$ of the integral equation (A2b) from that series by the Padé method. The iteration proceeds as follows:

$${}_\alpha\langle i'q'\chi'(I'j')|K_0|i_0 q_i\chi_i(I_0 j_i)\rangle_\alpha := {}_\alpha\langle i'q'\chi'(I'j')\Pi\mathcal{J}\mathcal{M}_\mathcal{J}\mathcal{T}\mathcal{M}_\mathcal{T}|PG_0(E_i+i0)|i_0 q_i\chi_i(I_0 j_i)\Pi\mathcal{J}\mathcal{M}_\mathcal{J}\mathcal{T}\mathcal{M}_\mathcal{T}\rangle_\alpha, \quad \text{(A4a)}$$

$${}_\alpha\langle i'q'\chi'(I'j')|K_{m+1}|i_0 q_i\chi_i(I_0 j_i)\rangle_\alpha \lambda^{m+1}$$
$$= \sum_{i'' i_\chi} \int q^2 dq\, {}_\alpha\langle i'q'\chi'(I'j')\Pi\mathcal{J}\mathcal{M}_\mathcal{J}\mathcal{T}\mathcal{M}_\mathcal{T}|PG_0(E_i+i0)|i'' q\chi(Ij)\Pi\mathcal{J}\mathcal{M}_\mathcal{J}\mathcal{T}\mathcal{M}_\mathcal{T}\rangle_\alpha$$
$$\times \lambda(i''|\mathbf{T}_\alpha(E_i+i0,q\chi(Ij))|i)\, {}_\alpha\langle iq\chi(Ij)|K_m|i_0 q_i\chi_i(I_0 j_i)\rangle_\alpha \lambda^m, \quad \text{(A4b)}$$

$$K^{(M)}(\lambda) = \sum_{m=0}^{M} K_m \lambda^m, \quad \text{(A4c)}$$

λ is an artificial strength parameter; the powers of λ count the number of times at which the two-baryon transition matrix acts on the initial channel state. The following subsections show how the Neumann series (A4c) is obtained and how the solution $K(\lambda)$ of the integral equation (A2b) is then constructed.

1. Spline interpolation

The Neumann series (A4c) is to be calculated at predetermined mesh points $\{q'\}$. However, the part

$${}_\alpha\langle i'q'\chi'(I'j')\Pi\mathcal{J}\mathcal{M}_\mathcal{J}\mathcal{T}\mathcal{M}_\mathcal{T}|PG_0(E_i+i0)$$
$$\times|iq\chi(Ij)\Pi\mathcal{J}\mathcal{M}_\mathcal{J}\mathcal{T}\mathcal{M}_\mathcal{T}\rangle_\alpha$$

of the integrand in Eq. (A4b) has moving singularities in its dependence on q. The nature of these singularities makes it necessary to access the integrand at untabulated arguments q. Therefore, an interpolation scheme becomes mandatory, which has to be accurate and efficient at the same time, since it will be used frequently for the K_m in the step (A4b) during

the buildup of the Neumann series (A4c). We use cubic spline interpolation to accomplish this task.

The q integration with the domain $[0,\infty)$ in Eq. (A4b) is carried out in two intervals $[0,q_{\rm sg}]$ and $[q_{\rm sg},\infty)$, $q_{\rm sg}=\sqrt{4mE_i/3}$ being the end point of the moving singularities. In the interval $[q_{\rm sg},\infty)$ the fixed set of predetermined mesh points $\{q'\}$ is used, in the interval $[0,q_{\rm sg}]$ the integrand, i.e., the part K_m of it, needs interpolation. For the description of the interpolation scheme we now return to a mathematical language denoting the dependence of K_m on q by the regular function $f(x)$. The function $f(x)$ needs interpolation, before the integration of Eq. (A4b) is carried out. In the interval $[0,q_{\rm sg}]$ we approximate the regular function $f(x)$, tabulated at the $n+1$ mesh points $\{x_0=0<x_1<\cdots<x_{n-1}<x_n=q_{\rm sg}\}$, by a set of piecewise cubic polynomials

$$S_i(x)=a_i+b_i(x-x_i)+c_i(x-x_i)^2+d_i(x-x_i)^3,$$
$$i=1,\ldots,n, \tag{A5}$$

where $S_i(x)$ is defined only within the interval $[x_{i-1},x_i]$. In each interval $f(x)\approx S_i(x)$ is assumed. The coefficients $\{a_i,b_i,c_i,d_i\}$ of the polynomials $S_i(x)$ are obtained by demanding the interpolation property

$$\forall i: S_i(x_{i-1})=f(x_{i-1})\wedge\ S_i(x_i)=f(x_i), \tag{A6a}$$

and the continuity of derivatives

$$\forall i (i<n): S_i'(x_i)=S_{i+1}'(x_i)\wedge\ S_i''(x_i)=S_{i+1}''(x_i). \tag{A6b}$$

Equations (A6) yield $2n+2(n-1)=4n-2$ conditions for the $4n$ unknown coefficients $\{a_i,b_i,c_i,d_i\}$. The two remaining conditions have to be supplied manually. We choose *natural* splines [18], i.e., we require $S_1''(x_0)=S_n''(x_n)=0$ or often alternatively as an additional check for stability *continuous third derivatives at* x_1 *and* x_{n-1}, i.e., in this case we require $S_1'''(x_1)=S_2'''(x_1)$ and $S_{n-1}'''(x_{n-1})=S_n'''(x_{n-1})$.

The coefficients $\{a_i,b_i,c_i,d_i\}$ depend linearly on the set of functions values $\{f(x_0),\ldots,f(x_n)\}$ [18]. We can therefore write

$$(a_0,b_0,c_0,d_0,\ldots,a_n,b_n,c_n,d_n)=[f(x_0),\ldots,f(x_n)]A^T \tag{A7}$$

with a matrix A^T that is solely determined by the mesh points x_i. In practice, A^T can easily be calculated, since Eqs. (A6) couple only neighboring splines.

Given A^T, the procedure of interpolating a particular function $f(x)$ to new arguments is as follows.

(1) Calculate the coefficients $\{a_i,b_i,c_i,d_i\}$ from the linear equation (A7).

(2) When interpolating the function $f(x)$ to the argument x, locate the particular interval $[x_{i-1},x_i]$ containing x. Since the mesh points x_i are kept in sorted order, binary search is used to obtain that interval in only $O(\ln n)$ steps in contrast to the $O(n)$ steps required by a linear search.

(3) Evaluate $S_i(x)$ and identify $f(x)=S_i(x)$.

Our particular feature of interpolation is the choice of different interpolation variables x in different intervals, i.e., q in the vicinity of 0, and $\sqrt{q_{\rm sg}^2-q^2}$ in the vicinity of $q_{\rm sg}$, the reason for the latter choice being the fact that the imaginary part of the propagator $\mathbf{T}_\alpha(E_i+i0)$ behaves in that limit as $\text{const}\sqrt{q_{\rm sg}^2-q^2}$. Those special choices greatly enhance the numerical accuracy. In the intermediate regime, interpolation in any of these variables works equally well.

2. Numerical integration

The iteration step (A4b) requires an integration on the magnitude q of the spectator momentum and a summation on form factor labels and on discrete quantum numbers. This subsection describes that integration on q.

In contrast to the contour-deformation technique of papers I and II, this paper uses real-axis integration. The integration has to deal with integrable singularities. The singularities arise in the kernel from the propagator $\mathbf{T}_\alpha(E_i+i0)$ and from the term $\langle\mathbf{g}_\alpha|PG_0(E_i+i0)|\mathbf{g}_\alpha\rangle$, whereas the driving term and K_m are regular in the integration variable. The propagator $\mathbf{T}_\alpha(E_i+i0)$ has a dynamic singularity, the deuteron bound-state pole in partial waves with the deuteron quantum numbers; that pole is rewritten as a δ function, immediately integrable, and a principal-part singularity which is regularized in standard fashion. Thus, the deuteron pole in the propagator $\mathbf{T}_\alpha(E_i+i0)$ deserves no further discussion here. The singularities in the term $\langle\mathbf{g}_\alpha|PG_0(E_i+i0)|\mathbf{g}_\alpha\rangle$ are also rewritten as a δ function, immediately integrable, and a principal-part singularity; its regularization is more involved; it is given in detail in Appendix D of Ref. [19]. After the regularization of the angular integration arising from the action of the permutation operator P, singularities in q integration remain; those singularities are dealt with in this subsection. The singularities of $\langle\mathbf{g}_\alpha|PG_0(E_i+i0)|\mathbf{g}_\alpha\rangle$ are of kinematical origin; they depend on both the initial and final spectator momenta q and q', called therefore moving singularities, but they are independent of the form factor labels and of discrete quantum numbers, except for baryonic content. In subsection 1 the integrand is interpolated for mesh points, which avoid the moving singularities. We therefore proceed as follows.

(1) The integrand in the iteration step (A4b) is split up into a sum of regular and singular functions. The integration of the regular integrand is not further discussed here, however, the one on the singular integrand. That singular integrand is factorized into a product of a regular function depending on the momenta, the form factor labels and the discrete quantum numbers, and a scalar function that carries all integrable singularities [19].

(2) The method of product integration [20–22] is used for the factorized integrand.

The employed real-axis integration technique is desribed for an integral of the form

$$I=\int_a^b dx w(x) f(x), \tag{A8a}$$

where $f:[a,b]\mapsto\mathbb{R}$ is a regular test function and

$w:[a,b]\mapsto\mathbb{R}$ is a function that carries the integrable singularities in (a,b). Also here we use standard mathematics notation, though we have the q integration of Eq. (A4b) in mind. For that integral (A8a) we seek a simple integration rule

$$I\approx\sum_{j=1}^{N} w_j f(x_j) \tag{A8b}$$

involving a given finite set $\{x_1,\ldots,x_N\}$ of mesh points with *weights* w_j to be determined. Note that the presence of the singular function $w(x)$ will be completely hidden in the weights w_j of the integration rule (A8b). Thus, once the weights are calculated, all occurring singular integrals can be as easily evaluated in the same way as the familiar Gauß-Legendre integration rule allows for regular functions.

The weights w_j are determined by first calculating the *moments*

$$\mu_k=\int_a^b dx w(x)h_k(x) \tag{A9}$$

for a set of basis functions $B=\{h_1(x),\ldots,h_N(x)\}$. The requirement that the integration rule (A8b) be exact for all functions $h_k(x)$ yields the linear system

$$\sum_{j=1}^{N} w_j h_k(x_j)=\mu_k \tag{A10}$$

for the unknown weights w_j. The set B is chosen in such a way that typical regular functions $f(x)$, as arising in the integration of Eq. (A4b), can be closely approximated by a linear combination of these basis functions $h_k(x)$. Since by construction all singularities are carried by $w(x)$ and the function $f(x)$ is regular, the basis functions $h_k(x)$ can simply be chosen to be linearly independent polynomials of order $(k-1)$. The resulting integration rule is therefore exact for all polynomials up to the degree $N-1$, i.e., deviations from exact integration are of the order $O(x^N)$.

Practically, the family of polynomials used for calculation of weights w_j from the linear system (A10) has to be chosen with care, in order to achieve numerical stability for the linear system (A10). For example if the polynomials are naively selected as powers, i.e., $B=\{1,x,x^2,\ldots,x^{N-1}\}$, the resulting linear system involves a Vandermonde matrix [23] and is ill conditioned. A much better conditioned linear system is obtained for a set of basis functions with an evenly distributed range of function values, e.g., the Chebyshev polynomials [20].

Note that we did not specify how to calculate the moments μ_k. The μ_k can be either obtained analytically or numerically, e.g., by using adaptive integration methods [24,25].

We close this subsection by giving an example. Since the singularities of the AGS equations are logarithmic we consider as example $w(x)=\ln x$ and choose the limits $a=0$, $b=+1$ for the integration domain. We use $f(x)=\cos x$ as the test function. The integral to be calculated is therefore

TABLE I. Comparison of integration techniques. The integral $I=\int_0^1 dx\,\ln x\cos x$ is evaluated by the subtraction technique (A12) and the integration rule (A10) for different numbers N of mesh points. The relative error $\Delta I=100|[I-\mathrm{Si}(1)]/\mathrm{Si}(1)|$ is given.

N	Gauß-Legendre with subtraction ΔI	Special weights according to Eq. (A10) ΔI
4	0.249612×10^{-02}	0.287699×10^{-02}
7	0.104399×10^{-03}	0.456670×10^{-07}
10	0.134596×10^{-04}	0.127911×10^{-11}
13	0.294369×10^{-05}	0.117349×10^{-13}

$$\int_0^1 dx\,\ln x\cos x=\mathrm{Si}(1), \tag{A11}$$

with $\mathrm{Si}(1)\approx-0.946\,083\,070\,367\,183\,014\,941\,353$, the sine integral, as analytical result. We compare the integration rule (A10) with the standard subtraction technique in Table (I). The subtraction technique regularizes the integral (A11) and evaluates it according to the Gauß-Legendre integration rule as follows:

$$\begin{aligned}\int_0^1 d\,x\,\ln x\cos x&=\int_0^1 dx\,\ln x[\cos x-\cos(0)]\\&\quad+\cos(0)\int_0^1 dx\,\ln x\\&\approx\sum_{j=1}^{N} w_j^{\mathrm{GL}}\ln x_j^{\mathrm{GL}}(\cos x_j^{\mathrm{GL}}-1)-1\end{aligned} \tag{A12}$$

with x_j^{GL} and w_j^{GL} denoting the Gauß-Legendre quadrature points and weights. The fast convergence of the integration rule (A10) is obvious from Table I and demonstrates its superiority over the standard Gauß-Legendre quadrature with subtraction.

3. Padé summation

In this subsection we carry out a construction of the solution $K(\lambda)$ of the integral equation (A2b) by the Padé method. We assume that the first terms of the Neumann series (A4c) of $K(\lambda)$ are known to us in the form

$$K^{(M)}(\lambda)=\sum_{m=0}^{M} K_m\lambda^m, \tag{A13}$$

according to Eq. (A4c). The Neumann series might not be globally convergent. The Padé method deals with the problem of nonconvergence or slow convergence by generating an approximating, better converging rational function $R(\lambda)=P(\lambda)/Q(\lambda)$ from the coefficients $\{K_m\}$ according to two conditions.

(1) Improved convergence is achieved by requiring the order of the denominator polynomial $Q(\lambda)$ to be equal or at

least close to the order of the numerator polynomial $P(\lambda)$. The convergence of the Neumann series is spoiled by poles in the complex plane. By introducing a rational approximation, which generates isolated poles in the complex plane, the behavior of the underlying function should be better approximated, as by the Neumann series.

(2) The rational function $R(\lambda)$ is required to be equivalent to $K^{(M)}(\lambda)$ up to the order in λ to which $K^{(M)}(\lambda)$ is defined, i.e., $|R(\lambda)-K^{(M)}(\lambda)|=O(\lambda^{M+1})$.

The reader has to keep in mind that all coefficients $\{K_m\}$ are vectors with respect to their dependence on the discretized set $\{q'\}$ of the continuous spectator momentum, on the rank label i' and on nonconserved discrete three-body quantum numbers $\chi'(I'j')$, the conserved three-body quantum numbers $\Pi\mathcal{J}\mathcal{M}_{\mathcal{J}}\mathcal{T}\mathcal{M}_{\mathcal{T}}$ being fixed. Thus, the numerator and denominator polynomials are constructed separately for each momentum q' and for each of the discrete labels and quantum numbers. We assume that all coefficients $\{K_m|m=1,\ldots,M\}$ are nonzero. In practice, this assumption is true except for the momentum $q'=0$ and particular quantum numbers. However, in this exceptional case *all* $\{K_m\}$ vanish due to geometric reasons; thus, there is no need for a Padé resummation. In our use of the Padé method, the approximating, better converging rational function $R(\lambda)$ is obtained in three steps.

The *first* step rewrites $K^{(M)}(\lambda)$ in form of a continued fraction $K_{\rm cf}^{(n)}(\lambda)$. Its definition is iterative, where the nth iteration is given by

$$K_{\rm cf}^{(n)}(\lambda)=K_0+\frac{a_1(\lambda)}{1+}\,\frac{a_2(\lambda)}{1+}\cdots\frac{a_n(\lambda)}{1+p^{(n)}(\lambda)/q^{(n)}(\lambda)} \tag{A14}$$

with

$$a_n(\lambda)=\alpha_n\lambda^{l(n)} \tag{A15}$$

being powers of order $l(n)$ in λ and $p^{(n)}(\lambda)$ and $q^{(n)}(\lambda)$ being polynomials in λ. The notation for a continued fraction is a standard one, e.g., as given in Ref. [24]. The quantities $a_{n+1}(\lambda)$, $p^{(n+1)}(\lambda)$, and $q^{(n+1)}(\lambda)$ are obtained from the corresponding quantities in the previous iteration step. $a_{n+1}(\lambda)$ is the lowest order term of $p^{(n)}(\lambda)$; $p^{(n+1)}(\lambda)$ and $q^{(n+1)}(\lambda)$ are obtained using the transformation of Viskovatov [26]

$$\begin{aligned}\frac{p^{(n)}(\lambda)}{q^{(n)}(\lambda)}&=\frac{a_{n+1}(\lambda)}{q^{(n)}(\lambda)[a_{n+1}(\lambda)/p^{(n)}(\lambda)]}\\&=\frac{a_{n+1}(\lambda)}{1+q^{(n)}(\lambda)[a_{n+1}(\lambda)/p^{(n)}(\lambda)]-1}\\&=\frac{a_{n+1}(\lambda)}{1+p^{(n+1)}(\lambda)/q^{(n+1)}(\lambda)},\end{aligned} \tag{A16}$$

with $q^{(n+1)}(\lambda)=p^{(n)}(\lambda)/a_{n+1}(\lambda)$ and $p^{(n+1)}(\lambda)=q^{(n)}(\lambda)-q^{(n+1)}(\lambda)$. The lowest-order term of any $q^{(n)}(\lambda)$ is always 1, the lowest-order term of any $p^{(n)}(\lambda)$ is at least of power 1. The iteration is started by putting $p^{(0)}(\lambda)=K^{(M)}(\lambda)-K_0$ and $q^{(0)}(\lambda)=1$; that starting step yields $a_1(\lambda)$, $p^{(1)}(\lambda)$, and $q^{(1)}(\lambda)$ for the continued fraction $K_{\rm cf}^{(1)}(\lambda)$ of lowest order. In each iteration step $K_{\rm cf}^{(n)}(\lambda)=K^{(M)}(\lambda)$. The iteration terminates after $2M$ steps at most, i.e., $p^{(2M)}(\lambda)=0$ and $a_{2M+1}(\lambda)=0$. Since also $K_{\rm cf}^{(2M)}(\lambda)=K^{(M)}(\lambda)$, the problem of nonconvergence still persists.

The exercise of continued fraction is only required to provide the quantities $a_n(\lambda)$ of Eq. (A15) for $n=1,\ldots,M$, which are needed for the later *second* step of constructing the rational function $R(\lambda)$. Our algorithm for the coefficients α_n in $a_n(\lambda)$ is derived from the continued fraction (A14) and runs as follows. We assume that the coefficients $\{\alpha_i|i=1,\ldots,m-1\}$ are determined from the coefficients $\{K_i|i=1,\ldots,m-1\}$; the determination of α_{m-1} requires auxiliary quantities $\{\gamma_i(m-1)|i=2,\ldots,m\}$ which are saved for the determination of α_m. The step from $(m-1)$ to m has three sequences.

(a)

$$\beta_1(m)=K_m, \tag{A17a}$$

$$\beta_i(m)=\gamma_i(m-1),\quad i=2,\ldots,m. \tag{A17b}$$

(b) The auxiliary quantities $\{\gamma_i(m)|i=2,\ldots,m+1\}$ are redefined by

$$\gamma_2(m)=0, \tag{A17c}$$

$$\gamma_{i+1}(m)=\frac{\beta_{i-1}(m)-\gamma_i(m)}{\alpha_{i-1}},\quad i=2,\ldots,m. \tag{A17d}$$

(c)

$$\alpha_m=\beta_m(m)-\gamma_{m+1}(m). \tag{A17e}$$

The algorithm does not need to determine the power $l(n)$ of λ in $a_n(\lambda)$ of Eq. (A15), since the rational function $R(\lambda)$ will be considered only for $\lambda=1$.

In the *second* step the rational function $R(\lambda)$ is generated by a recurrence relation for the polynomials $P^{(n)}(\lambda)$ and $Q^{(n)}(\lambda)$

$$P^{(n)}(\lambda)=P^{(n-1)}(\lambda)+a_n(\lambda)P^{(n-2)}(\lambda), \tag{A18a}$$

$$Q^{(n)}(\lambda)=Q^{(n-1)}(\lambda)+a_n(\lambda)Q^{(n-2)}(\lambda), \tag{A18b}$$

which is started by

$$P^{(-1)}(\lambda)=1,\quad Q^{(-1)}(\lambda)=0, \tag{A18c}$$

$$P^{(0)}(\lambda)=K_0,\quad Q^{(0)}(\lambda)=1. \tag{A18d}$$

The recurrence relations (A18) were first derived by Wallis in 1655 [27]. The recurrence uses the functions $a_n(\lambda)$ of the continued fraction $K_{\rm cf}^{(n)}(\lambda)$. It terminates at $n=n_{\max}$ when $a_{n_{\max}+1}(\lambda)=0$. However, if the natural termination of the continued fraction were used, i.e., $n_{\max}=2M$ (in exceptional cases $n_{\max}<2M$), nothing would be gained; in that case $P^{(2M)}(\lambda)=K^{(M)}(\lambda)$ and $Q^{(2M)}(\lambda)=1$. If, however, the con-

tinued fraction is terminated at $n_{\max}=M$ putting $a_{M+1}(\lambda)=0$, the rational function $R(\lambda)$ satisfies the two desired properties, spelt out at the beginning of this subsection. The construction of the rational function $R(\lambda)$ in the second step appears awkward, since it is based on the continued fraction of the first step. However, it is chosen, since it is numerically stable, in contrast to other possible techniques.

In the *third* step the convergence of the Padé summation is checked. We are satisfied with the obtained approximating rational function $R(\lambda)$, if for a given order M of the Neumann series the deviation of the complete vectors is small in successive orders, i.e., $||P^{(M)}(\lambda)/Q^{(M)}(\lambda)-P^{(M-1)}(\lambda)/Q^{(M-1)}(\lambda)||_{\lambda=1}<\epsilon$, ϵ being our required accuracy. Computer economy calls for as small a number M as reasonable. The number M is found by starting the accuracy check already for $M=1$; the Neumann series (A4c) is carried to a higher order $M+1$, requiring a repetition of the steps one to three only when that accuracy check fails. The actual number M used depends on the scattering energy as well as on the total three-body quantum numbers of ${}_\alpha\langle i'q'\chi(I'j')\Pi\mathcal{J}\mathcal{M}_\mathcal{J}\mathcal{T}\mathcal{M}_\mathcal{T}|G_0(E_i+i0)U(E_i+i0)G_0(E_i+i0)|i_0q_i\chi_i(I_0j_i)\Pi\mathcal{J}\mathcal{M}_\mathcal{J}\mathcal{T}\mathcal{M}_\mathcal{T}\rangle_\alpha$.

[1] S. Nemoto, K. Chmielewski, J. Haidenbauer, S. Oryu, P.U. Sauer, and N.W. Schellingerhout, Few-Body Syst. **24**, 213 (1998).

[2] C. Hajduk, P.U. Sauer, and W. Strueve, Nucl. Phys. **A405**, 581 (1983).

[3] S. Nemoto, K. Chmielewski, J. Haidenbauer, U. Meyer, S. Oryu, and P.U. Sauer, Few-Body Syst. **24**, 241 (1998).

[4] Y. Koike and J. Haidenbauer, Nucl. Phys. **A463**, 365c (1987).

[5] W. Glöckle, H. Witała, D. Hüber, H. Kamada, and J. Golak, Phys. Rep. **274**, 107 (1996).

[6] S. Nemoto, K. Chmielewski, S. Oryu, and P.U. Sauer, Phys. Rev. C **58**, 2599 (1998).

[7] M. Lacombe, B. Loiseau, J.M. Richard, R. Vinh Mau, J. Coté, P. Pirès, and R. de Tourreil, Phys. Rev. C **21**, 861 (1980).

[8] *Polarization Phenomena in Nuclear Reactions*, edited by H. H. Barshall and W. Haeberli (University of Wisconsin, Madison, 1970), p. xxv.

[9] M. Allet *et al.*, Phys. Rev. C **50**, 602 (1994).

[10] J. Strate *et al.*, Nucl. Phys. **A501**, 51 (1989).

[11] G. Rauprich, S. Lemaitre, P. Niessen, K.R. Nyga, R. Reckenfelderbäumer, L. Sydow, H. Paetz gen. Schieck, H. Witała, and W. Glöckle, Nucl. Phys. **A535**, 313 (1991).

[12] A. Deltuva, K. Chmielewski, and P. U. Sauer (unpublished).

[13] L.M. Qin *et al.*, Nucl. Phys. **A587**, 252 (1995).

[14] J. Jourdan (unpublished); S. Buttazzoni, Ph.D. thesis, Universität Basel, 1999, http://jazz.physik.unibas.ch/Dissertationen.html.

[15] J. Zejma *et al.*, Phys. Rev. C **55**, 42 (1997).

[16] M. Allet *et al.*, Few-Body Syst. **20**, 27 (1996).

[17] K. Bodek *et al.*, Nucl. Phys. **A631**, 687c (1998).

[18] C. de Boor, *A Practical Guide to Splines* (Springer-Verlag, New York, 1978).

[19] K. Chmielewski, Ph.D. thesis, Universität Hannover, 1999, URL http://edok01.tib.uni-hannover.de/edoks/e002/26544327X.pdf

[20] I.H. Sloan and W.E. Smith, Numer. Math. **34**, 387 (1980).

[21] W.E. Smith and I.H. Sloan, SIAM (Soc. Ind. Appl. Math.) J. Numer. Anal. **17**, 1 (1980).

[22] P. Rabinowitz and I.H. Sloan, SIAM (Soc. Ind. Appl. Math.) J. Numer. Anal. **21**, 149 (1984).

[23] P. A. Fuhrmann, *A Polynomial Approach to Linear Algebra* (Springer, New York, 1996).

[24] W. H. Press, S. A. Teukolsky, W. T. Vetterling, and B. P. Flannery, *Numerical Recipes in C*, 2nd ed. (Cambridge University Press, Cambridge, 1992).

[25] W. H. Press, S. A. Teukolsky, W. T. Vetterling, and B. P. Flannery, *Numerical Recipes in Fortran 90* (Cambridge University Press, Cambridge, 1996).

[26] C. T. Fike, *Computer Evaluation of Mathematical Functions* (Prentice-Hall, Englewood Cliffs, NJ, 1968).

[27] J. Wallis, *Arithmetica Infinitorum* (Oxford, 1655), (reprinted by Georg Olms Verlag, Hildesheim, 1972).